Maintaining intact parathyroid glands throughout life requires Dicer and microRNA-mediated mTORC1 signaling

Alia Hassan[1*], Nariman Khalaily[1*], Rachel Kilav-Levin[1,2], Barbara Del Castello[3,4], Nancy Ruth Manley[3,5], Iddo Z. Ben-Dov[6] and Tally Naveh-Many[1,7]

[1]Minerva Center for Bone and Mineral Research, Nephrology Services, Hadassah Hebrew University Medical Center and Faculty of Medicine,
Jerusalem, Israel
[2]School of Nursing, Jerusalem College of Technology, Faculty of Life and Health Sciences, Jerusalem, Israel
[3]Department of Genetics, University of Georgia, Athens, GA, USA, 30602
[4]Current address: CRDF Global, Arlington VA, USA, 22202
[5]Current address: School of Life Sciences, Arizona State University, Tempe, AZ, USA, 85281
[6]Laboratory of Medical Transcriptomics, Nephrology Services, Hadassah Hebrew University Medical Center and Faculty of Medicine, Jerusalem,
Israel
[7]Wohl Institute for Translational Medicine, Hadassah Hebrew University Medical Center, Jerusalem, Israel.

*Equal contributing authors

Abstract

Parathyroid hormone (PTH) is central for mineral metabolism and bone strength. Secondary hyperparathyroidism (SHP) frequently accompanies chronic kidney disease (CKD), contributing to morbidity and mortality in patients. Our previous findings demonstrated that PT-*Dicer*$^{-/-}$ mice, with parathyroid specific deletion of *Dicer* and consequently microRNA, maintained normal serum PTH levels but failed to increase serum PTH in response to hypocalcemia and CKD, the major inducers of PTH secretion. Additionally, we elucidated a critical role of mTORC1 in CKD-induced SHP. We now explored the roles of Dicer and mTORC1 in parathyroid development and function. Despite normal serum PTH levels, PT-*Dicer*$^{-/-}$ mice displayed apoptotic loss of intact parathyroid glands postnatally, which were subsequently replaced by scattered cell clusters, and reduced mTORC1 activity. Accordingly, PT-*mTORC1*$^{-/-}$ mice exhibited the absence of intact parathyroid glands, while retaining normal serum PTH levels, similar to PT-*Dicer*$^{-/-}$ mice. Conversely, PT-*Tsc1*$^{-/-}$ mice with hyperactivated mTORC1 exhibited enlarged glands and elevated serum PTH and calcium levels. Notably, PT-*Dicer*$^{-/-}$;*Tsc1*$^{-/-}$ double knockout mice demonstrated a reversal of PT-*Dicer*$^{-/-}$ aparathyroidism, preserving intact parathyroid glands and reinstating CKD-induced SHP. These findings imply that mTOR operates downstream of Dicer and miRNA depletion. Moreover, Dicer, miRNA and mTORC1 are crucial to postnatal parathyroid gland integrity and function.

Introduction

Parathyroid hormone (PTH) determines serum calcium levels and bone strength [1-3]. Secondary hyperparathyroidism (SHP) is a common complication of chronic kidney disease (CKD) that correlates with patient morbidity and mortality [4, 5]. In experimental SHP, the elevation in PTH gene expression is attributed to post-transcriptional mechanisms due to enhanced PTH mRNA stability [6, 7]. An additional layer of post-transcriptional control is mediated by microRNA (miRNA). miRNA are initially transcribed as longer precursor RNA molecules that are ultimately cleaved in the cytoplasm by Dicer to form mature and functional miRNA [8]. Dysregulated miRNA profiles have been observed in patients with primary hyperparathyroidism, presenting differentially expressed miRNA in parathyroid adenomas and carcinomas when compared to normal parathyroid tissue [9, 10]. In an earlier investigation, we demonstrated through miRNA sequencing that human and rodent parathyroids share similar miRNA profiles. Moreover, a significantly disrupted miRNA transcriptome was observed in hyperplastic parathyroid glands from end-stage renal disease patients with SHP, as well as in mice and rats with experimentally-induced CKD-associated SHP resulting from a high-phosphorus adenine diet [11]. Antagonizing two abundant parathyroid miRNA, let-7 and miR-148, led to alterations in serum PTH levels in both normal kidney controls and CKD rats, along with changes in PTH secretion in isolated parathyroid glands in vitro, pointing to the direct impact of these miRNA on regulation of PTH gene expression [11]. To study the global role of miRNA in the parathyroid, we generated mice with targeted gene deletion of *Dicer* and consequently miRNA dysregulation specifically in their parathyroid glands. Remarkably, PT-*Dicer*$^{-/-}$ mice developed normally and had normal basal serum PTH, calcium and phosphate levels. However, PT-*Dicer*$^{-/-}$ mice failed to increase serum PTH levels in response to the stimuli of acute and chronic hypocalcemia and CKD, underscoring the central roles of parathyroid *Dicer* and miRNAs in mediating the responses of the parathyroid to the major PTH secretion stimulators [12].

Mechanistic target of rapamycin (mTOR) plays a major role in regulating different cellular processes, including growth and metabolism. mTOR functions as two distinct complexes, mTORC1 and mTORC2 [13]. mTORC1 is a key regulator of cell growth and metabolism and exerts its influence by integrating cues such as growth factors, energy levels, cellular stress, and amino acids [14]. The promotion of

protein synthesis by mTORC1 largely depends on the phosphorylation of two key effectors, ribosomal protein S6 (S6) and eukaryotic translation initiation factor 4E (eIF4E)-binding protein (4EBP) [13, 15]. Phosphorylation of S6 (pS6) is used as an indicator of mTORC1 activity, playing a beneficial role in protein synthesis and control of cell size. In a prior study, we have demonstrated the activation of parathyroid mTORC1 signaling in SHP. Furthermore, we found that the inhibition of mTORC1 using rapamycin not only prevented but also corrected parathyroid cell proliferation in SHP rats both in vivo and in parathyroid glands in cultures in vitro [16]. Tuberous sclerosis complex (TSC) genes, *Tsc1 and Tsc2*, encode for hamartin and tuberin proteins, forming the TSC complex that negatively regulates mTORC1. Mutations in either *Tsc1* or *Tsc2* lead to mTORC1 hyperactivation, associated with cellular growth abnormalities and tumorigenesis [17-19]. TSC syndrome is a rare autosomal dominant disorder that affects multiple organ systems. Bone mineral disturbances remain relatively unrecognized in TSC syndrome, as do alterations in calcium homeostasis [20]. Limited reports exist regarding serum PTH levels and their alteration in TSC syndrome, with only a single case of elevated serum PTH described in a TSC syndrome patient [20].

This study investigates the interplay between miRNA and mTORC1 in parathyroid function, employing genetically modified mouse models featuring parathyroid-specific deletions of *Dicer* (PT-*Dicer*$^{-/-}$ mice), *mTORC1* (PT-*mTORC1*$^{-/-}$ mice) or *Tsc1* (PT-*Tsc1*$^{-/-}$ mice, characterized by mTORC1 hyperactivation). Additionally we investigated the combined effects of *Dicer* and *Tsc1* deletions in double knockout mice (PT-*Dicer*$^{-/-}$;*Tsc1*$^{-/-}$ mice). Our findings underscore the essential roles of Dicer, miRNA and mTORC1 signaling in maintaining the lifelong integrity and functionality of parathyroid glands, as well as in the context of CKD-induced SHP development.

Results

Parathyroid-specific PT-*Dicer*$^{-/-}$ mice exhibit undetectable or severely hypoplastic parathyroid glands

Accurately identifying the minute parathyroid glands embedded within the thyroid of adult mice proves challenging, even when utilizing a binocular microscope. To study the parathyroids of PT-*Dicer*$^{-/-}$ and PT-*Dicer*$^{+/+}$ mice, we therefore initially employed immunohistochemistry (IHC) on serial thyroparathyroid paraffin sections stained for

PTH. In most mature control mice, the two parathyroid glands were readily identifiable (**Fig 1A-C**). Missing glands were likely ectopically located, as previously reported in ~30% of mice (**Fig 1C**) [21]. Unexpectedly, intact parathyroid glands could not be discerned in any of the sections from PT-*Dicer*$^{-/-}$ mice (n=65) (**Fig 1C**). In the few sections that displayed PTH-producing cells, these cells formed small, disorganized structures of cell clumps with PTH expression, very different from the intact well-defined parathyroids in control mice (**Fig 1A and B**). Histological analysis using H&E staining of parathyroid sections demonstrated the preservation of the parathyroid gland capsule in PT-*Dicer*$^{-/-}$ mice, yet adipocytes infiltrated and occupied the void left by the ablated parathyroid cells (**Fig 1B**). It is plausible that in sections from the majority of PT-*Dicer*$^{-/-}$ mice, where PTH-producing cells were not detected, the minute cell clumps were too small to be detected by IHC. Therefore, mature PT-*Dicer*$^{-/-}$ mice lack intact parathyroid glands and instead exhibit residual parathyroid cell clusters.

Deletion of *Dicer* and consequently miRNA in the parathyroid does not affect the volume of embryonic parathyroid glands or their expression of PTH and caspase3

The initiation of PTH expression starts as early as embryonic day E11.5 [22], implying that the human PTH promoter-driven *Cre* would result in early embryonic *Dicer* disruption in PT-*Dicer*$^{-/-}$ embryos. To follow the development of parathyroid glands during fetal stages, PT-*Dicer*$^{-/-}$ and control PT-*Dicer*$^{+/+}$embryos were generated by timed mating and studied at E13.5, E19.5 and E21.5. Immunofluorescence (IF) staining for PTH in paraffin-embedded whole embryo sections at all embryonic ages consistently revealed two intact parathyroid glands in both PT-*Dicer*$^{-/-}$ and control embryos with no difference in PTH staining between PT-*Dicer*$^{-/-}$ and control mice at any of the time points. Apoptotic cell death detection by cleaved caspase 3 also showed no difference between PT-*Dicer*$^{-/-}$ and control mice (**Fig 1D and Supplemental Fig 1A&B**). Likewise, volumetric analysis of the parathyroids demonstrated no disparity (**Fig 1E** and **Supplemental Fig 1C&D**). Hence, our findings indicate that the presence of Dicer and thus miRNA is not imperative for embryonic parathyroid development and for *Pth* embryonic expression, and that the loss of intact parathyroid glands in PT-*Dicer*$^{-/-}$ mice occurs after E21.5.

Parathyroid glands are gradually lost after birth in PT-*YFP;Dicer*$^{-/-}$ mice, due to increased apoptosis

To enhance the identification and tracking of parathyroid cells and cell clusters in whole mice, we generated mice with parathyroid-specific YFP labeling using *Cre-Lox* recombination in either control *Dicer*$^{+/+}$ or PT-*Dicer*$^{-/-}$ mice. The PT-*YFP;Dicer*$^{-/-}$ mice expressing YFP exhibited normal basal serum levels of calcium, phosphate and PTH, comparable to control PT-*YFP;Dicer*$^{+/+}$ mice (**Supplemental Fig 2A-D, control diet**) [12], mirroring the findings previously described in PT-*Dicer*$^{-/-}$ mice lacking YFP expression [12, 16]. Renal failure induced by an adenine-rich high phosphorus diet led to the expected changes in serum biochemistry in both YFP expressing strains (**Supplemental Fig 2A-C**). However, PT-*YFP;Dicer*$^{-/-}$ did not increase in serum PTH levels compared to the expected rise seen in control PT-*YFP;Dicer*$^{+/+}$ mice (**Supplemental Fig 2D**), mirroring the findings previously described in PT-*Dicer*$^{-/-}$ mice without YFP expression [12, 16]. Therefore, PT-*YFP;Dicer* $^{-/-}$ mice manifest the same characteristics as PT-*Dicer*$^{-/-}$ mice, which includes normal basal PTH levels and inability to increase serum PTH in kidney failure.

We then proceeded to monitor the development of parathyroid glands in both control PT-*YFP*;*Dicer*$^{+/+}$ and PT-*YFP*;*Dicer*$^{-/-}$ mice, following them from birth to adulthood. Fluorescence-guided microscopy of the exposed neck area easily detected two intact parathyroid glands in control mice across all ages, with the majority of glands located near the superior or inferior poles of the thyroid (**Fig 2A&B**). Notably, immediately after birth, at P0 (not shown) and P1, PT-*YFP;Dicer*$^{-/-}$ pups also exhibited the presence of two glands (**Fig 2A&B**). However, from P2 onward, a progressive reduction in the number of parathyroid glands was observed in PT-*YFP;Dicer*$^{-/-}$ mice, with the left gland persisting longer. By P12, there were no visible intact parathyroid glands in the neck area of PT-*YFP;Dicer*$^{-/-}$ mice (**Fig 2A&B**). Therefore, our findings affirm that mice with parathyroid-specific deletion of *Dicer* are initially born with intact parathyroid glands that are subsequently lost shortly after birth, thus confirming the essential role of miRNA postnatally in the preservation of intact parathyroid glands.

IF staining for cleaved caspase 3 of parathyroid gland sections from control PT-*YFP;Dicer*$^{-+/+}$ and PT-*YFP;Dicer*$^{-/-}$ mice, at P1 and P4, showed increased occurrence of apoptosis in parathyroid glands from PT-*YFP;Dicer*$^{-/-}$ neonates. There was no change in staining for PTH or for the specific parathyroid markers glial cells missing 2 (GCM2) and calcium sensing receptor (CaSR) in PT-*YFP;Dicer*$^{-/-}$ compared to control PT-*YFP;Dicer*$^{+/+}$ pups (**Fig 2C&D**). Taken together, our

findings demonstrate that the deletion of *Dicer* and the consequent global miRNA deficiency triggers apoptosis in parathyroid cells shortly after birth. This ultimately leads to the loss of intact parathyroid glands in PT-*Dicer*$^{-/-}$ mice with no change in serum PTH levels or in the expression of parathyroid markers within the surviving cells.

The residual parathyroid cell clusters in PT-*Dicer*$^{-/-}$ mice still express *Dicer* and adequate PTH production for maintaining basal serum levels

To ascertain the origin of PTH production responsible for maintaining normal serum levels in PT-*YFP;Dicer*$^{-/-}$ mice, we performed thyroidectomy in both control and PT-*YFP;Dicer*$^{-/-}$ mice. Thyroidectomy involved the removal of the thyroid glands along with any associated parathyroid glands in control mice, and the extirpation of any lingering parathyroid cell clusters within PT-*YFP;Dicer*$^{-/-}$ mice (**Fig 3A**). As anticipated, thyroparathyroidectomy led to a reduction in serum PTH levels within 30 minutes in control PT-*YFP*;*Dicer*$^{+/+}$ mice [23]. Intriguingly, a similar decrease in serum PTH levels was observed following thyroidectomy in PT-*YFP;Dicer*$^{-/-}$ mice (**Fig 3B**). This result indicates that PTH producing cells are located within the thyroid of these mice and play a substantial role in maintaining basal serum PTH levels in PT-*YFP;Dicer*$^{-/-}$ mice. Thus, normal basal serum PTH levels observed in PT-*Dicer*$^{-/-}$ mice, which lack intact parathyroid glands, is produced by the small parathyroid cell clusters located within the thyroid gland.

To characterize the cell clusters still present in PT-*Dicer*$^{-/-}$ mice that express and secrete PTH, we performed RNAscope in situ hybridization (ISH). This technique enables the imaging of individual RNA molecules within individual cells of tissue sections. As expected, control PT-*Dicer*$^{+/+}$ mice expressed *PTH* and *GCM2* mRNAs throughout the parathyroid, as well as the targeted *Dicer* sequence. Conversely, most parathyroid cells in PT-*Dicer*$^{-/-}$ mice showed no expression for these transcripts at 2 months of age, confirming the successful deletion of *Dicer* and the subsequent absence of intact parathyroid glands. Nevertheless, small cell clusters still retained *Pth*, *Gcm2*, and *Dicer* expression in PT-*Dicer*$^{-/-}$ mice (**Fig 3C** and **Supplemental Fig 3**). This suggests that *Dicer* and miRNA ablation leads to death of parathyroid cells. However, a subset of cells evade *Dicer* deletion allowing for their survival while preserving their parathyroid traits and functions. As a result, the outcome of parathyroid-specific *Dicer* and miRNA ablation is the death of parathyroid cells and

loss of parathyroid glands, which is mitigated by a small subpopulation of parathyroid cells evading *Dicer* deletion.

PT-*tdTomato;Dicer*$^{-/-}$ mice reveal the gradual loss of parathyroid glands

The small clusters of parathyroid cells in adult PT-*YFP;Dicer*$^{-/-}$ mice were barely identifiable by IF staining and whole mouse parathyroid *YFP* imaging (**Fig 1A&B and Fig 2A, P12**). To enhance the visibility of these structures, we generated an additional mouse colony introducing the brighter *tdTomato* fluorescence marker, initially in conjunction with *YFP*, generating parathyroid *Cre*-driven control PT-*YFP;dTomat;Dicer*$^{+/+}$ and PT-*YFP;dTomat;Dicer*$^{-/-}$ mice. The parathyroids were readily distinguishable in control mice using both *YFP* and *tdTomato* fluorescence guided microscopy, with the *tdTomato* signal being significantly more intense than that of *YFP* (**Fig 4A**). As above, we could not detect intact parathyroid glands in adult PT-*YFP;tdTomato;Dicer*$^{-/-}$ mice (**Figs 4A, 2 and 1**). However, with tdTomato imaging, the presence of tiny parathyroid cell clusters became more apparent, which were not detectable with *YFP* in PT-*YFP;tdTomato;Dicer*$^{-/-}$ mice (**Fig 4A**).

The enhanced intensity of the *tdTomato* signal revealed the timeframe for the progressive degeneration of parathyroid glands in PT-*tdTomato*;*Dicer*$^{-/-}$ mice. In PT-*tdTomato*;*Dicer*$^{-/-}$ mice, the reduced intensity of the *tdTomato* signal was already visible at P1, when gland size was still comparable to that of the control mice (**Fig 4B&C**). Remnants of parathyroid glands were still visible even at P25 with the tdTomato reporter, although exhibiting diminished density and a more punctate morphology when contrasted with the parathyroids of control mice (**Fig 4B**). Taken together, these findings show that PT-*Dicer*$^{-/-}$ mice are born with intact parathyroid glands that are gradually lost after birth. Parathyroid cell clusters that still express *Dicer* maintain normal serum PTH levels in PT-*Dicer*$^{-/-}$ mice.

Reduced parathyroid mTORC1 pathway activity in PT-*Dicer*$^{-/-}$ mice

We have previously demonstrated the activation of the parathyroid mTORC1 pathway in rats with CKD-induced SHP. Additionally, we found that mTORC1 inhibition by rapamycin prevented and corrected parathyroid cell proliferation in these rats [16]. We therefore assessed the impact of *Dicer* and miRNA ablation on the parathyroid mTORC1 pathway. Indeed, phosphorylated ribosomal protein S6 (pS6) (Ser235/236), a marker for mTORC1 activity, decreased in parathyroid extracts derived from PT-*Dicer*$^{-/-}$ mice compared to baseline levels in control mice at P1, the stage when the parathyroid glands were still intact (**Fig 5A-B**). A similar decrease in pS6 was

observed by IF staining of parathyroid sections of adult PT-*Dicer*$^{-/-}$ compared to control mice showing the reduction in pS6 staining within the remaining parathyroid cell clusters in these mice (**Fig 5C-D**). Hence, deletion of *Dicer* and miRNA results in diminished parathyroid mTORC1 pathway activity, suggesting that *Dicer* and miRNA ablation could impact the mTORC1 pathway in PT-*Dicer*$^{-/-}$ mice.

PT-*mTORC1*$^{-/-}$ mice lack intact parathyroid glands from early after birth, yet maintain normal serum PTH levels, similar to PT-*Dicer*$^{-/-}$ mice

To study the effect of decreased mTORC1 pathway activity on the morphology of parathyroid glands we generated mice with parathyroid specific ablation of m*TORC1* and *td-Tomato* expression (PT-*mTORC1*$^{-/-}$ mice). The PT-*mTORC1*$^{-/-}$ mice developed normally, and were viable and fertile. Survival of the PT-*mTORC1*$^{-/-}$ mice was similar to that of control littermates as measured up to 1 year (not shown). There were also no differences in serum calcium (0.60 ±0.01 mmol/L in control and 0.58 ±0.03 mmol/L in PT-*mTORC1*$^{-/-}$ mice, n=12 in each group) and phosphate levels (0.85 ±0.07 mmol/L control and 0.74 ±0.04 mmol/L PT-*mTORC1*$^{-/-}$ mice, n=5 in each group) in PT-*mTORC1*$^{-/-}$ mice compared to control PT-*mTORC1*$^{+/+}$ mice both at 3 months and other time points (data not presented). Serum PTH levels were similar to controls at all ages tested (**Fig 6C**).

Fluorescence guided microscopy showed two intact parathyroid glands in PT-*mTORC1*$^{-/-}$ mice at P11 and at earlier stages (**Fig 6A** and not shown), similar to control PT-*mTORC1*$^{+/+}$ mice. However, beginning at ~P11 onward, a progressive reduction in gland size ensued, characterized by a punctuated appearance, ultimately resulting in the absence of intact glands in fully adult PT-*mTORC1*$^{-/-}$ mice. Remarkably, these mice maintained normal serum biochemical profiles and PTH levels (**Fig 6A&C**). The remnant cell clusters in PT-*mTORC1*$^{-/-}$ mice were also evident within thyroparathyroid sections, as revealed by H&E staining (**Fig 6B**). There was no change in PTH content in the remnant parathyroids of PT-*mTORC1*$^{-/-}$ compared to the intact glands of control mice as indicated by the intensity of IF staining in thyroparathyroid sections (**Supplemental Fig 4A&B**), presumably because PTH was actively secreted to compensate for the decreased parathyroid cell mass. Interestingly, there was a decrease in PTH mRNA with no change in CaSR mRNA in parathyroids of PT-*mTORC1*$^{-/-}$ mice at 3 and 4 months (**Supplemental Fig 5** and not shown). Hence, *mTORC1* ablation yields smaller, disrupted parathyroid tissue soon after birth. Remarkably, despite the lack of intact glands and reduction in

the number of PTH producing cells, PT-*mTORC1*$^{-/-}$ mice maintain normal serum PTH levels, mirroring the phenotype seen in PT-*Dicer*$^{-/-}$ mice in the context of *Dicer* ablation.

Parathyroid-specific *Tsc1*$^{-/-}$ mice exhibit enlarged parathyroid glands and increased serum PTH and calcium levels

To gain deeper insights into the contribution of *mTORC1* in the parathyroid, we generated mice with parathyroid-specific mTORC1 hyperactivation through ablation of the mTOR repressor, TSC1, combined with tdTomato expression. mTORC1 was indeed activated in the parathyroids of PT-*TSC1*$^{-/-}$ mice, as indicated by increased pS6 (Ser235/236) IF staining (**Supplemental Fig 6**). The PT-*TSC1*$^{-/-}$ mice developed normally and did not display gross physical abnormalities. However, there was a pronounced reduction in the survival rate of PT-*TSC1*$^{-/-}$ mice when compared to their control littermates, as observed from 1 month to 1 year and depicted in **Fig 7A**. Unlike controls, only a single PT-*TSC1*$^{-/-}$ mouse survived up to 11 months. Serum PTH levels in PT-*TSC1*$^{-/-}$ mice were increased 1.5-fold at 1 month when the glands were already enlarged, and continued to increase with age (**Fig 7B**). Serum calcium levels were increased at both 3 and 5 month consistent with the high serum PTH levels (**Fig 7C**). The premature mortality observed in PT-*TSC1*$^{-/-}$ mice is likely attributed to the hyperparathyroidism induced hypercalcemia, similar to the increased mortality in primary hyperparathyroidism patients with increased serum calcium levels [24].

Fluorescence guided microscopy in PT-*TSC1*$^{-/-}$ mice revealed parathyroid glands of similar size to those of control PT-*TSC1*$^{+/+}$ mice at P2. However, from P8 onward, PT-*TSC1*$^{-/-}$ pups had visibly larger parathyroid glands compared to controls, which persisted and escalated substantially over time (**Fig 7D and Supplemental Fig 7**). Parathyroid gland 2-dimensional measurements reaffirmed these results. At 3 months, parathyroid glands in PT-*TSC1*$^{-/-}$ mice displayed a 4-fold increase in size compared to those of control PT-*TSC1*$^{+/+}$ mice. This enlargement continued to escalate, reaching 6 times the size of controls at the 5-month (**Fig 7E and Supplemental Fig 8**). Thus, mTORC1 hyperactivation does not influence parathyroid embryonic development but instead exerts its effects after birth, leading to an increase in parathyroid gland dimensions.

PTH mRNA levels were increased in PT-*TSC1*$^{-/-}$ mice with an in-consistent increase in CasR mRNA (**Supplemental Fig 9**). Of interest, the rise in PTH mRNA

corresponded to the elevation in serum PTH levels, although it remained notably milder than the evident enlargement in gland size. Serum PTH levels also only partially mirrored the substantial growth in gland size (**Fig 7B&E**). Taken together, hyperactivation of mTORC1 in PT-*TSC1*$^{-/-}$ mice leads to a significant enlargement of the parathyroid glands, coupled with increased serum PTH and calcium levels, underscoring the pivotal role of mTORC1 in parathyroid gland morphology and parathyroid cell survival.

Parathyroid-specific *Dicer* and *TSC1* double knockout reverses the aparathyroidism of PT-*Dicer*$^{-/-}$ mice and restores their CKD induced SHP

To further affirm the miRNA-mTORC1 axis in the parathyroid, we generated parathyroid specific double knockout mice with ablation of both *Dicer* and *TSC1* and *td-Tomato* expression (PT-*Dicer*$^{-/-}$;*TSC1*$^{-/-}$ mice). Remarkably, PT-*Dicer*$^{-/-}$;*TSC1*$^{-/-}$ mice exhibited intact parathyroid glands comparable in size to those of control mice, in contrast to PT-*Dicer*$^{-/-}$ mice. This observation was consistent at 2 months of age and across all ages examined up to 9 months (**Fig 8A** and not shown). Serum PTH levels in PT-*Dicer*$^{-/-}$;*TSC1*$^{-/-}$ mice were also similar to those of control mice. Importantly, the simultaneous ablation of both *Dicer* and *TSC1* not only salvaged the structural integrity of the parathyroid glands, but also reinstated their capacity to elevate serum PTH levels in response to adenine high-phosphorus-induced CKD (**Fig 8B**). Hence, the findings from PT-*Dicer*$^{-/-}$;*TSC1*$^{-/-}$ mice underscore that *TSC1* ablation effectively overrides the lack of parathyroid glands observed in PT-*Dicer*$^{-/-}$ mice. This highlights the hierarchical relationship between Dicer and miRNA ablation and their subsequent influence on mTORC1 activity downstream, affecting parathyroid gland integrity and function.

Discussion

The present study underscores the pivotal roles of Dicer, miRNA, and the mTORC1 signaling pathway in the maintaining intact parathyroid glands throughout the mouse lifespan. Our prior work utilizing parathyroid-specific *Dicer* knockout (PT-*Dicer*$^{-/-}$ mice), illuminated the importance of Dicer and miRNA in stimulating the parathyroid during both acute and chronic hypocalcemia and uremic conditions [12]. Building on this PT-*Dicer*$^{-/-}$ mouse model, we now reveal an unexpected consequence of *Dicer* and miRNA deficiency - the postnatal apoptosis-driven loss of intact parathyroid glands shortly after birth. This leads to the emergence of scattered clumps of PTH-

producing cells in adult mice. This intriguing revelation underscores the non-essential role of Dicer and miRNA in embryonic parathyroid development, while emphasizing their vital function in preserving postnatal and lifelong structural integrity of the parathyroid glands. As previously reported, serum PTH levels in these mice remained within the normal range, suggesting that these dispersed cell clusters adequately produce PTH to maintain basal PTH levels.

The transcription factor *Gcm2*, is expressed during both developmental stages and in the adult [25]. In humans, *GCM2* loss of function mutations cause idiopathic and familial hypoparathyroidism [26]. Various mouse models have shown that *Gcm2* null mutations cause aparathyroidism in the fetal and adult mouse [27-29]. As opposed to *GCM2*-knockout mice in which parathyroid cells undergo apoptosis by E12 [28], PT-*Dicer*$^{-/-}$ mice described in this study are born with intact glands that undergo apoptosis shortly after birth, gradually leading to the disappearance of the glands and eventual absence of intact parathyroid glands post day P12. We employed three strains of parathyroid-specific *Dicer* ablation: PT-*Dicer*$^{-/-}$, PT-*YFP;Dicer*$^{-/-}$, and PT-*tdTomato;Dicer*$^{-/-}$, along with respective control mice to demonstrate that adult PT-*Dicer*$^{-/-}$ mice across all strains lack intact parathyroid glands, replaced by scattered clumps of parathyroid cells in the thyroid tissue or neck area (more effectively detected using the sensitive tdTomato marker). Notably, *GCM2* expression remained unchanged in the parathyroids of PT-*Dicer*$^{-/-}$ mice. These parathyroid cell clusters appear sufficient to maintain normal basal PTH and calcium levels in PT-*Dicer*$^{-/-}$ mice, even in the absence of intact parathyroid glands. Thyroidectomy in PT-*Dicer*$^{-/-}$ mice led to decreased PTH levels similar to control mice, where intact parathyroid glands were removed along with the thyroid. The origin of the cell clusters in PT-*Dicer*$^{-/-}$ mice remains unclear. RNAscope analysis indicated that these cells still express *Dicer*, *Pth*, and *Gcm2*. The incomplete *Cre*-mediated *Dicer* deletion may arise from variable *Cre* expression or its expression in distinct parathyroid cell populations at different time point. Different cell populations having different requirements for Dicer, or a gradual turnover of cells as they progress through a sensitive part of the cell cycle may be the cause for the gradual loss of cells postnatally. Consequently, only cells failing to delete *Dicer* could survive, retaining parathyroid identity and function. The outcome of *Dicer* and miRNA ablation therefore is death of parathyroid cells, resulting in a condition of aparathyroidism. The survival of some cells post-apoptosis could explain the milder phenotype compared to complete parathyroid cell

loss due to *Dicer* ablation. These scattered clusters seemingly provide sufficient basal serum PTH through excessive PTH production, potentially rendering them unresponsive to further stimulation by hypocalcemia or CKD [12]. An alternative explanation could be that the impaired structure or smaller cell mass of the hypoplastic parathyroids hinders their ability to further elevate serum PTH levels. Indeed, studies have demonstrated the critical role of intact parathyroid tissue architecture in the direct effect of high phosphate on stimulating PTH secretion [30, 31].

Aberrant miRNA regulation has been associated with various parathyroid-related diseases, such as primary hyperparathyroidism and CKD-induced SHP. Altered miRNA profiles have been detected in parathyroid adenomas and carcinomas, implying their potential role in these conditions [10]. Through parathyroid miRNA deep sequencing, we have previously shown shared profiles between human and rodent parathyroids. Moreover, there were altered miRNA profiles in parathyroid glands from uremic and normal rats as well as in glands form CKD-related SHP patients compared to patients with normal renal function. The manipulating of specific dysregulated miRNAs in experimental SHP using antagomir oligonucleotides has been shown to modify PTH secretion both in vivo and in vitro [11]. Evolutionary conservation of miRNAs in normal parathyroid glands and their dysregulation in SHP underscore their significance in parathyroid function and hyperparathyroidism development [11, 32]. Here we point to miRNA target genes and pathways crucial for parathyroid gland morphology and function.

The interaction between miRNAs and the mTOR pathway, wherein miRNAs can either inhibit or stimulate mTOR signaling, is well documented [33, 34]. For example, in Xenopus development, inhibiting miRNA biogenesis resulted in reduced size of the pronephric kidney, attributed to decreased mTORC1 activity [33, 35]. Notably, the involvement of mTORC1 signaling extends to the realm of parathyroid gland biology. Genomic alterations in the PI3K/AKT/mTOR and Wnt signaling pathways have been associated with parathyroid carcinoma [36-38]. Moreover, mutations in the *Tsc1* gene, leading to mTORC1 hyperactivation, correlate with enlarged parathyroid glands and elevated serum PTH levels [39, 40]. In experimental rat models of CKD-induced SHP, parathyroid mTORC1 signaling activation has been documented. Pharmacological inhibition of mTORC1 effectively prevented and reversed parathyroid cell proliferation, while also halting the increase in PTH secretion in these rats [16].

We have now demonstrated that loss of *Dicer* in PT-*Dicer*$^{-/-}$ mice leads to a decrease in mTORC1 activity, suggesting a sequential relationship between the two. Indeed, PT-*mTORC1*$^{-/-}$ mice lacked intact parathyroid glands after birth, but preserved normal PTH levels, comparable to those observed in *PT-Dicer*$^{-/-}$ mice. Conversely, PT-*Tsc1*$^{-/-}$ mice with mTORC1 hyperactivation exhibited enlarged glands and increased serum PTH and calcium levels. These findings underscore the pivotal role of the mTORC1 pathway in upholding the structural integrity of the parathyroid glands. The precise mechanism through which mTOR signaling influences parathyroid gland integrity and the survival of parathyroid cells remains to be elucidated. Importantly, in PT-*Dicer*$^{-/-}$*;Tsc1*$^{-/-}$ mice with dual *Dicer* and *TSC1* ablation, intact glands were preserved, overriding the aparathyroidism state associated with *Dicer* deletion. Moreover, unlike PT-*Dicer*$^{-/-}$ mice, PT-*Dicer*$^{-/-}$*;Tsc1*$^{-/-}$ mice demonstrated increased serum PTH levels in the context of CKD-induced SHP. Thus, the PT-*Dicer*$^{-/-}$;*TSC1*$^{-/-}$ mice demonstrate that *TSC1* ablation effectively supersedes the absence of parathyroid glands seen in PT-*Dicer*$^{-/-}$ mice. This observation further underscores the hierarchical relationship between Dicer, miRNA, and mTORC1, implying that Dicer and miRNA operate upstream of mTORC1. Collectively, our results indicate that the ablation of *Dicer* and miRNA leads to a reduction in mTORC1 pathway activity, ultimately culminating in the demise of parathyroid glands (**Fig 8C&D**). Dicer, miRNA, and mTORC1 emerge as vital contributors to the maintenance of parathyroid gland integrity postnatally, as well to the development of CKD-induced SHP, shedding light on their importance in parathyroid cell survival and function and highlighting new avenues for understanding and potentially treating parathyroid-related disorders.

Materials and Methods

Animal housing

All animal experiments were approved by the Institutional Animal Care and Use Committee of the Hadassah Hebrew University. Animals had free access to food and drinking water.

Parathyroid-specific knockout mice

Parathyroid-specific *Dicer* knockout mice (PT-*Dicer*$^{-/-}$) were generated by Cre-LoxP recombination using PTH-*Cre* mice, which express the *Cre* recombinase under the control of the human parathyroid hormone (PTH) promoter [FVBTg(PTH-

Cre); Jackson Laboratory, Bar Harbor, ME] [41], as previously described [12]. To visualize the small mouse parathyroid glands using fluorescence microscopy, we introduced EYFP or tdTomato labeling. *EYFP* expression was achieved by crossing mice from both control PT-*Dicer*$^{+/+}$ and PT-*Dicer*$^{-/-}$ strains with *Rosa26 loxP*-STOP-*loxP EYFP* mutant mice (129X1-*Gt(ROSA)26Sor*$^{tm1(EYFP)Cos}$/J), from Jackson Laboratory, Bar Harbor, ME). This resulted in *Cre*-dependent *EYFP* expression specifically in the parathyroids (PT-*YFP;Dicer*$^{+/+}$ and PT-*YFP;Dicer*$^{-/-}$ mice). To enhance the detection of the small parathyroid cell clusters that were difficult to identify in YFP-expressing PT-*YFP;Dicer*$^{-/-}$ and PT-*mTORC1*$^{-/-}$ mice, we utilized the more intense tdTomato labeling. For this purpose, mice with a modified *Rosa26* locus17 were used, where the *Rosa26* locus contained a targeted insertion of a construct encompassing the strong and ubiquitously expressed *CAG* promoter, followed by a *loxP* stop cassette-controlled *tdTomato* marker gene [42]. Consequently, the resulting mice exhibited specific *tdTomato* expression in the parathyroids.

Parathyroid-specific *mTORC1* knockout mice (PT-*mTORC1*$^{-/-}$) and Parathyroid-specific *TSC1* knockout mice (PT-*TSC1*$^{-/-}$) were generated by crossing PTH-*Cre* mice with mice possessing floxed *mTORC1* [43, 44] *or TSC1* genes [43, 45], respectively. The appropriate strains were further crossbred to generate the *Dicer* and *TSC1* double knockout mice and their appropriate control mice (PT-*Dicer*$^{+/+}$;*Tsc1*$^{+/+}$ and PT-*Dicer*$^{-/-}$;*Tsc1*$^{-/-}$ mice). All control mice were littermates that were *Cre*-positive and had the appropriate wild type (wt) alleles for *Dicer*, *mTORC1* and *TSC1*.

Genotyping

Total DNA was extracted from ear samples obtained from the offspring and genotyping was conducted using standard PCR techniques to identify the presence of PTH-*Cre* and *Dicer loxP*, *YFP* and *tdTomato* alleles using the appropriate primers (Table 1) [12].

Table 1. Primers used for DNA genotyping.

Genes	Sequence (5'-3')
PTH-*Cre*	Fw: TGCCACGACCAAGTGACAGC Rev: CCAGGTTACGGATATAGTTCATG
Dicer loxP	Fw: CCTGACAGTGACGGTCCAAAG Rev: CATGACTCTTCAACTCAAACT
YFP	ROSA 26R: AAAGTCGCTCTG AGTTGTTAT

	BTG 60: GAAAGACCGCGAAGAGTT TG BTG 62: TAAGCCTGCCCAGAAGACTC
tdTomato wt	Fw: AAGGGAGCTGCAGTGGAGTA Rev: CCGAAAATCTGTGGGAAGTC
tdTomato loxP	Fw: CTGTTCCTGTACGGCATGG Rev: GGCATTAAAGCAGCGTATCC
mTOR loxP	Fw: TTATGTTTGATAATTGCAGTTTTGGCTAG Rev: TTAGGACTCCTTCTGTGACATACATTTC
TSC loxP	Fw: AGGAGGCCTCTTCTGCTACC Rev: CAGCTCCGACCATGAAGTG

Serum biochemistry and PTH levels

Mice were anesthetized using a ketamine-xylazine solution, and blood samples were obtained from the abdominal aorta using heparin tubes. Following coagulation, the blood samples were centrifuged at 3000 g for 10 minutes to separate the serum, which was then isolated and stored at 20° C. Serum samples were analyzed using QuantiChrom kits (BioAssay Systems, Hayward, CA) to measure serum calcium and blood urea nitrogen (BUN) levels. In specific experiments, total serum calcium levels were determined using the Atellica CH Calcium kit (Tarrytown, NY). Serum PTH levels were measured using a mouse Intact 1–84 PTH ELISA kit (Quidel, Athens, OH) [12].

Thyroparathyroidectomy

The thyroparathyroidectomy procedure involved the removal of the thyroid gland along with the embedded parathyroid glands in control mice, or the parathyroid cell clusters as seen in PT-Dicer-/- mice. The mice, aged between 5 to 6 weeks, were anesthetized via intraperitoneal injection (IP) of ketamine-xylazine solution. A ventral midline incision was made in the neck area, and the brown adipose and muscle tissues were carefully retracted. Under a binocular microscope, the thyroids were located, exposed, and excised using fine scissors. Following the removal of the thyroid tissue, a sterile gauze was applied to the neck area, and the mice were kept warm under red light. For the sham-operated mice, the same procedure was performed, except the thyroids were spared. Thirty minutes after the thyroidectomy, blood samples were collected from both the thyroidectomized and sham-operated mice [23]. To confirm the

successful removal of parathyroid-containing thyroid tissue in control mice, fluorescent-guided microscopy of the exposed neck was performed. Fluorescent-guided microscopy confirmed that PT-*YFP;Dicer*$^{-/-}$ mice lacked parathyroid glands altogether.

RNA isolation and qRT-PCR

Thyroparathyroid tissue was excised as above, rapidly frozen in liquid nitrogen and stored at -80° C to maintain its integrity. To extract total RNA from the two parathyroid glands of individual mice, 400 µl of TRIzol Reagent (Ambion, Carlsbad, CA) was utilized. The tissue was homogenized using a bead-beater, and RNA extraction was carried out in accordance with the manufacturer's instructions. The resulting RNA pellet was resuspended in 20 µl of RNase-free water, and 10 µl of the resuspended RNA was used for cDNA synthesis using a qScript cDNA Synthesis Kit (Quanta Bio, Beverly, MA). Subsequently, quantitative (q) PCR analysis was conducted using the PerfeCTa SYBR Green FastMix, Low ROX (Quanta Bio) in the ViiA 7 Fast Real-Time PCR System (Applied Biosystems, Waltham, MS). The primers used for qRT-PCR were for mouse PTH: Fw: 5'-ATCCCTTTGAGAGTCATTG-3' and Rev: 5'-GTTTGGGTAAGAAGACAGAC-3'; mouse calcium sensing receptor: Fw: 5'-GAGTGCATCAGGTATAACTTC-3' and Rev: 5'- GTGTTACAGGTGTCGAATATC-3' and mouse β-actin: Fw: 5'-CCTAGGCACCAGGGTGTGAT-3' and Rev: 5'-TCAGGGTCAGGATACCTCTCTTG-3' [12].

Microscope fluorescent imaging and quantification

Postnatal mice at various ages, ranging from P1 to adult, were anesthetized, and under bright field illumination, a surgical incision was made in the neck area to expose the thyroparathyroid. The parathyroid glands of PT-*YFP* or PT-*tdTomato* mice were visualized using GFP or CY3 filters, respectively, on a Nikon SMZ25 stereomicroscope. The exposure time for YFP fluorescence was set at 2 seconds, while for tdTomato, it was either 67 or 250 milliseconds as indicated, depending on the specific experiment requirements. The microscope images presented are composite images where the GFP or CY3 fluorescent signals were overlaid on bright field (BF) light images. To quantify the intensity of the fluorescent parathyroid gland images, ImageJ software (NIH, Bethesda, MD) was employed.

Immunofluorescence staining of mouse paraffin sections

Mouse thyroparathyroid glands were excised and fixed in 4% formaldehyde solution overnight. Subsequently the fixed glands were embedded in paraffin, and 6 µm-thick sections were prepared for further analysis. After rehydration, antigens were retrieved by pressure cooker (121° C for 3 min) in 20 mM citric acid buffer (pH= 6). Immunostaining was performed overnight at 4° C using primary antibodies for PTH (1:400, Bio-Rad, Hercules, CA), Cleaved caspase 3 (1:200, Cell Signaling Technology Danvers, MA), GCM2 (1:1000, Abcam, Cambridge, UK) CaSR (1:1500, Novus Biologicals, Littleton, CO), and phosphorylated ribosomal protein S6 (pS6) (S235/236) (1:500, Cell Signaling Technology) all diluted in Cas block (Zymed Laboratories, San Francisco, CA). Fluor chrome–conjugated secondary antibodies Cy3 and Cy5 (Bethyl, Montgomery, TX) and SYTOX nuclear staining (Life Technologies, Carlsbad, CA) were used for detection. Images were obtained using a Fluoview 1000 Olympus florescence microscope.

Parathyroid gland size and *tdTomato* signal intensity

The size of the parathyroid glands and the intensity of the fluorescent images were measured using ImageJ software (NIH, Bethesda, MD). 2D size estimation was performed on bright field images to avoid effects of the high intensity of tdTomato florescence (Supplemental Fig 8).

Immunofluorescence staining of mouse embryos

Embryos were obtained from timed matings at different stages of fetal parathyroid development. The day when a vaginal plug was observed was designated as embryonic day (E) 0.5. Embryos were collected on specific days of interest (E13.5, E19.5, and E21.5) and their developmental stage was determined based on somite counts and morphological features. For immunofluorescence (IF) staining, 8 µm-thick serial sections of paraffin-embedded embryos, which were fixed in 4% paraformaldehyde (PFA), were used. The slides were subjected to staining for PTH (Quidel), CC3 (Cell Signaling Technology), and nuclear staining with DAPI. Embryos for paraffin sections to be used in RNAscope analysis were fixed in a 4% paraformaldehyde solution overnight. Subsequently, they were thoroughly washed with PBS, dehydrated in a series of ethanol dilutions, permeabilized using xylene, and finally embryos were embedded in paraffin wax. All steps were performed using RNase-free reagents. Sections for RNAscope analysis were sliced at 5 µm. IHC was performed using antibodies for PTH (Quidel 21-2310), CASPASE 3 (Cell Signaling Technologies 9661S), both of which were diluted at 1:200 and DAPI nuclear staining.

Using IHC-generated images, three-dimensional (3D) reconstructions of the parathyroids were created utilizing the WinSurf® software. These reconstructions enabled the generation of volumetric data for all collected parathyroids. The embryos were examined at three developmental stages: E13.5, E19.5, and E21.5. To quantify the size of the parathyroid domain, the sum of all areas (in pixels) within a pouch was calculated. These calculations were then entered into Prism© software for subsequent statistical analysis. The statistical significance was determined using an unpaired T-test. For the E13.5, a total of 8 control embryos (16 parathyroids) and 15 mutant embryos (30 parathyroids) were examined using IHC. Among these, 4 control parathyroids and 7 mutant parathyroids were quantified. Similarly, for the E19.5 stage, 4 control embryos (8 parathyroids) and 7 mutant embryos (14 parathyroids) were subjected to IHC analysis. Quantification was performed on 4 control parathyroids and 5 mutant parathyroids. At the E21.5 stage, 5 control embryos (10 parathyroids) and 6 mutant embryos (12 parathyroids) were examined.

RNAscope in situ hybridization

RNAscope analysis was conducted on RNase-free paraformaldehyde-fixed, paraffin-embedded sections following the protocols and utilizing the reagents provided by the manufacturer RNAscope™ (ACDbio, Newark, CA) [46]. The specific probes used included Gcm2, PTH and Dicer.

Statistical analysis

Values are presented as mean±SE. A 2-tailed Student's t-test was used to assess differences among groups. A p value of less than 0.05 was considered significant.

Acknowledgments

We thank Oded Volovelsky and Moris Nechama (Department of Pediatric Nephrology, Hadassah Hebrew University Medical Center and Faculty of Medicine, Jerusalem, Israel) for providing the *mTORC1* and *Tsc1* floxed mice and for valuable discussions and insight; Jie Li (Department of Genetics, University of Georgia, Athens, GA, USA, 30602, current address: NIAID, Bethesda, MD, USA, 20892) for additional technical assistance; E. Piontek, for technical assistance in paraffin embedding and tissue sectioning (Hadassah Hebrew University Medical Center, Israel). T. Naveh-Many is a research associate of the Wohl's Translation Research Institute at Hadassah Hebrew University Medical Center.

Funding

This work was supported by grants from the Israel Science Foundation (ISF 642/16 to T.N.-M.) and the United States-Israel Binational Science Foundation (BSF 2019300 to T.N.-M., N.R.M and I.Z.B.-D.).

References

1. Hofer AM, Brown EM: Extracellular calcium sensing and signalling. *NatRevMolCell Biol,* 4**:** 530-538, 2003
2. Pollack MR, Brown EM, Chou Y-HW, Hebert SC, Marx SJ, Steinman B, et al.: Mutations in the human Ca^{2+} -sensing receptor gene cause familial hypocalciuric hypercalcemia and neonatal severe hyperparathyroidism. *Cell,* 75**:** 1297-1303, 1993
3. Naveh-Many T, Silver J: Regulation of parathyroid hormone gene expression by hypocalcemia, hypercalcemia, and vitamin D in the rat. *JClinInvest,* 86**:** 1313-1319, 1990
4. Hannan FM, Kallay E, Chang W, Brandi ML, Thakker RV: The calcium-sensing receptor in physiology and in calcitropic and noncalcitropic diseases. *Nature Reviews Endocrinology,* 15**:** 33-51, 2019 10.1038/s41574-018-0115-0
5. Silver J, Kilav R, Naveh-Many T: Mechanisms of secondary hyperparathyroidism. *AmJPhysiol Renal Physiol,* 283**:** F367-F376, 2002
6. Moallem E, Silver J, Kilav R, Naveh-Many T: RNA protein binding and post-transcriptional regulation of PTH gene expression by calcium and phosphate. *J Biol Chem,* 273**:** 5253-5259, 1998
7. Nechama M, Uchida T, Yosef-Levi IM, Silver J, Naveh-Many T: The peptidyl-prolyl isomerase Pin1 determines parathyroid hormone mRNA levels and stability in rat models of secondary hyperparathyroidism. *The Journal of clinical investigation,* 119**:** 3102-3114, 2009
8. Lee Y, Ahn C, Han JJ, Choi H, Kim J, Yim J, et al.: The nuclear RNase III Drosha initiates microRNA processing. *Nature,* 425**:** 415-419, 2003
9. Corbetta S, Vaira V, Guarnieri V, Scillitani A, Eller-Vainicher C, Ferrero S, et al.: Differential expression of microRNAs in human parathyroid carcinomas compared with normal parathyroid tissue. *Endocrine-related cancer,* 17**:** 135-146, 2010
10. Wielogórska M, Podgórska B, Niemira M, Szelachowska M, Krętowski A, Siewko K: MicroRNA Profile Alterations in Parathyroid Carcinoma: Latest Updates and Perspectives. *Cancers (Basel),* 14**:** 876, 2022 10.3390/cancers14040876
11. Shilo V, Mor-Yosef Levi I, Abel R, Mihailović A, Wasserman G, Naveh-Many T, et al.: Let-7 and MicroRNA-148 Regulate Parathyroid Hormone Levels in Secondary Hyperparathyroidism. *Journal of the American Society of Nephrology,* 28**:** 2353-2363, 2017 10.1681/asn.2016050585
12. Shilo V, Ben Dov IZ, Nechama M, Silver J, Naveh-Many T: Parathyroid-specific deletion of dicer-dependent microRNAs abrogates the response of the parathyroid to acute and chronic hypocalcemia and uremia. *FASEB Journal,* 29**:** 3964-3976, 2015
13. Saxton RA, Sabatini DM: mTOR Signaling in Growth, Metabolism, and Disease. *Cell,* 168**:** 960-976, 2017 10.1016/j.cell.2017.02.004
14. Condon KJ, Sabatini DM: Nutrient regulation of mTORC1 at a glance. *Journal of cell science,* 132, 2019 10.1242/jcs.222570

15. Kim YC, Guan KL: mTOR: a pharmacologic target for autophagy regulation. *The Journal of clinical investigation,* 125**:** 25-32, 2015 10.1172/jci73939
16. Volovelsky O, Cohen G, Kenig A, Wasserman G, Dreazen A, Meyuhas O, et al.: Phosphorylation of Ribosomal Protein S6 Mediates Mammalian Target of Rapamycin Complex 1-Induced Parathyroid Cell Proliferation in Secondary Hyperparathyroidism. *JAmSocNephrol,* 27**:** 1091-1101, 2016 ASN.2015040339 [pii];10.1681/ASN.2015040339 [doi]
17. De Waele L, Lagae L, Mekahli D: Tuberous sclerosis complex: the past and the future. *Pediatric Nephrology,* 30**:** 1771-1780, 2015 10.1007/s00467-014-3027-9
18. Mallela K, Kumar A: Role of TSC1 in physiology and diseases. *Molecular and cellular biochemistry,* 476**:** 2269-2282, 2021 10.1007/s11010-021-04088-3
19. Tee AR, Manning BD, Roux PP, Cantley LC, Blenis J: Tuberous sclerosis complex gene products, Tuberin and Hamartin, control mTOR signaling by acting as a GTPase-activating protein complex toward Rheb. *Current biology : CB,* 13**:** 1259-1268, 2003 10.1016/s0960-9822(03)00506-2
20. Kim K, Kim S, Na KY, Chae DW, Chin HJ: Severe Hypocalcemia in a Patient with Tuberous Sclerosis Complex. *Electrolyte & blood pressure : E & BP,* 17**:** 21-24, 2019 10.5049/ebp.2019.17.1.21
21. Au - Bi R, Au - Fan Y, Au - Luo E, Au - Yuan Q, Au - Mannstadt M: Two Techniques to Create Hypoparathyroid Mice: Parathyroidectomy Using GFP Glands and Diphtheria-Toxin-Mediated Parathyroid Ablation. *JoVE***:** e55010, 2017 doi:10.3791/55010
22. Manley NR: Embryology of the Parathyroid Glands. In: *Hypoparathyroidism.* edited by Brandi ML, Brown EM, Milano, Springer Milan, 2015, pp 11-18
23. Lavi-Moshayoff V, Wasserman G, Meir T, Silver J, Naveh-Many T: PTH increases FGF23 gene expression and mediates the high-FGF23 levels of experimental kidney failure: a bone parathyroid feedback loop. *American Journal of Physiology - Renal Physiology,* 299**:** F882-F889, 2010
24. Wermers RA, Griebeler ML, Thapa P, Hathcock MA, Kearns AE: Survival in primary hyperparathyroidism over five decades (1965-2010) a population-based retrospective study. *Bone,* 152**:** 116099, 2021 10.1016/j.bone.2021.116099
25. Canaff L, Zhou X, Mosesova I, Cole DE, Hendy GN: Glial Cells Missing-2 (GCM2) transactivates the calcium-sensing receptor gene: effect of a dominant-negative GCM2 mutant associated with autosomal dominant hypoparathyroidism. *HumMutat,* 30**:** 85-92, 2008
26. Canaff L, Guarnieri V, Kim Y, Wong BYL, Nolin-Lapalme A, Cole DEC, et al.: Novel Glial Cells Missing-2 (GCM2) variants in parathyroid disorders. *European Journal of Endocrinology,* 186**:** 351-366, 2022 10.1530/EJE-21-0433
27. Gunther T, Chen ZF, Kim J, Priemel M, Rueger JM, Amling M, et al.: Genetic ablation of parathyroid glands reveals another source of parathyroid hormone. *Nature,* 406**:** 199-203, 2000
28. Liu Z, Yu S, Manley NR: Gcm2 is required for the differentiation and survival of parathyroid precursor cells in the parathyroid/thymus primordia. *Dev Biol,* 305**:** 333-346, 2007 10.1016/j.ydbio.2007.02.014
29. Yuan Z, Opas EE, Vrikshajanani C, Libutti SK, Levine MA: Generation of mice encoding a conditional null allele of Gcm2. *Transgenic Research,* 23**:** 631-641, 2014 10.1007/s11248-014-9799-7
30. Almaden Y, Canalejo A, Hernandez A, Ballesteros E, Garcia-Navarro S, Torres A, et al.: Direct effect of phosphorus on parathyroid hormone secretion from whole rat parathyroid glands in vitro. *J Bone Miner Res,* 11**:** 970-976, 1996

31. Nielsen PK, Feldt-Rasmusen U, Olgaard K: A direct effect of phosphate on PTH release from bovine parathyroid tissue slices but not from dispersed parathyroid cells. *NephrolDialTransplant,* 11**:** 1762-1768, 1996
32. Shilo V, Silver J, Naveh-Many T: Micro-RNAs in the parathyroid: a new portal in understanding secondary hyperparathyroidism. *Current opinion in nephrology and hypertension,* 25**:** 271-277, 2016
33. Nazari N, Jafari F, Ghalamfarsa G, Hadinia A, Atapour A, Ahmadi M, et al.: The emerging role of microRNA in regulating the mTOR signaling pathway in immune and inflammatory responses. *Immunology & Cell Biology,* 99**:** 814-832, 2021 https://doi.org/10.1111/imcb.12477
34. Romaker D, Kumar V, Cerqueira DM, Cox RM, Wessely O: MicroRNAs are critical regulators of tuberous sclerosis complex and mTORC1 activity in the size control of the Xenopus kidney. *Proc Natl Acad Sci U S A,* 111**:** 6335-6340, 2014 10.1073/pnas.1320577111
35. Zhang Y, Huang B, Wang HY, Chang A, Zheng XFS: Emerging Role of MicroRNAs in mTOR Signaling. *Cellular and molecular life sciences : CMLS,* 74**:** 2613-2625, 2017 10.1007/s00018-017-2485-1
36. Kong SH: Updates of Genomics and Proteomics of Parathyroid Carcinoma. *Endocrines,* 3**:** 745-752, 2022
37. Hu Y, Zhang X, Wang O, Bi Y, Xing X, Cui M, et al.: The genomic profile of parathyroid carcinoma based on whole-genome sequencing. *International journal of cancer,* 147**:** 2446-2457, 2020
38. Marini F, Giusti F, Palmini G, Aurilia C, Donati S, Brandi ML: Parathyroid carcinoma: molecular therapeutic targets. *Endocrine*, 2023 10.1007/s12020-023-03376-w
39. Kang H, Pettinga D, Schubert AD, Ladenson PW, Ball DW, Chung JH, et al.: Genomic Profiling of Parathyroid Carcinoma Reveals Genomic Alterations Suggesting Benefit from Therapy. *The oncologist,* 24**:** 791-797, 2019 10.1634/theoncologist.2018-0334
40. Kutahyalioglu M, Nguyen HT, Kwatampora L, Clarke C, Silva A, Ibrahim E, et al.: Genetic profiling as a clinical tool in advanced parathyroid carcinoma. *Journal of cancer research and clinical oncology,* 145**:** 1977-1986, 2019 10.1007/s00432-019-02945-9
41. Libutti SK, Crabtree JS, Lorang D, Burns AL, Mazzanti C, Hewitt SM, et al.: Parathyroid gland-specific deletion of the mouse Men1 gene results in parathyroid neoplasia and hypercalcemic hyperparathyroidism. *Cancer Res,* 63**:** 8022-8028, 2003
42. Madisen L, Zwingman TA, Sunkin SM, Oh SW, Zariwala HA, Gu H, et al.: A robust and high-throughput Cre reporting and characterization system for the whole mouse brain. *Nature neuroscience,* 13**:** 133-140, 2010 10.1038/nn.2467
43. Volovelsky O, Nguyen T, Jarmas AE, Combes AN, Wilson SB, Little MH, et al.: Hamartin regulates cessation of mouse nephrogenesis independently of Mtor. *Proc Natl Acad Sci U S A,* 115**:** 5998-6003, 2018 10.1073/pnas.1712955115
44. Gangloff YG, Mueller M, Dann SG, Svoboda P, Sticker M, Spetz JF, et al.: Disruption of the mouse mTOR gene leads to early postimplantation lethality and prohibits embryonic stem cell development. *Molecular and cellular biology,* 24**:** 9508-9516, 2004 10.1128/mcb.24.21.9508-9516.2004
45. Kwiatkowski DJ, Zhang H, Bandura JL, Heiberger KM, Glogauer M, el-Hashemite N, et al.: A mouse model of TSC1 reveals sex-dependent lethality from liver hemangiomas, and up-regulation of p70S6 kinase activity in Tsc1 null cells. *Human molecular genetics,* 11**:** 525-534, 2002 10.1093/hmg/11.5.525
46. Chen D, Wang X, Liang D, Gordon J, Mittal A, Manley N, et al.: Fibronectin signals through integrin α5β1 to regulate cardiovascular development in a cell type-specific manner. *Developmental Biology,* 407**:** 195-210, 2015 https://doi.org/10.1016/j.ydbio.2015.09.016

Figure legends

Figure 1. Aberrant parathyroid tissue in mature adult PT-*Dicer*$^{-/-}$ but not in PT-*Dicer*$^{+/+}$ embryos. (A) Representative immunofluorescence staining of thyroparathyroid sections from control (PT-*Dicer*$^{+/+}$) and parathyroid-specific *Dicer*$^{-/-}$ (PT-*Dicer*$^{-/-}$) mice highlighting sections with detectable parathyroid cells, stained for nuclear sytox (green), PTH (blue) and merge images. **(B)** Histological sections stained with H&E from PT-*Dicer*$^{+/+}$ and PT-*Dicer*$^{-/-}$ mice. **(C)** Percent of mice with 2 intact parathyroid glands detected in serial sections of thyroparathyroids from PT-*Dicer*$^{+/+}$ (n=45) and PT-*Dicer*$^{-/-}$ mice (n=65). (**D**) Representative IF staining for PTH and cleaved caspase 3 of parathyroids from control PT-*Dicer*$^{+/+}$ and PT-*Dicer*$^{-/-}$ embryos at E13.5. (**E**) Volumetric analysis of parathyroid embryos as in D (PT-*Dicer*$^{+/+}$ n=5, PT-*Dicer*$^{-/-}$ n=7 parathyroids).

Figure 2. Intact parathyroid glands are gradually lost after birth in PT-*YFP;Dicer*$^{-/-}$ mice, as evident by YFP fluorescent microscopy, attributed to increased apoptosis. (**A**) Representative fluorescent microscope images superimposed on bright field images of exposed glands in the neck area of control PT-*YFP;Dicer*$^{+/+}$ and PT-*YFP;Dicer*$^{-/-}$ mice at postpartum days P1, P12 and P35. The fluorescence intensity exposure was 2 seconds, with a magnification x2. T, thyroid, PT, parathyroid, Tr, trachea. Arrows point to the location of parathyroid glands or cell clusters. (**B**) Percentage of mice with either 2 intact parathyroid glands or no intact glands at each time point as in A including in adult mice (>35 days to 1 year) (n=6-18, >35 n= 20-44). (**C**) Representative IF staining of paraffin sections from parathyroid glands of P1 (n=2-4) control PT-*YFP*;*Dicer* $^{+/+}$ and PT-*YFP*;*Dicer* $^{-/-}$ mice stained for cleaved caspase 3 (red), PTH (blue) and nuclear sytox (green). (**D**) Representative IF staining of paraffin sections from parathyroid glands of P4 control PT-*YFP*;*Dicer* $^{+/+}$ and PT-*YFP*;*Dicer* $^{-/-}$ mice stained for CaSR (blue), GCM2(red) and nuclear sytox (green) (n=2-4).

Figure 3. Serum PTH levels are similarly decreased following thyroidectomy in control PT-*YFP;Dicer* $^{+/+}$ and PT-*YFP;Dicer* $^{-/-}$ mice. (**A**) Thyroidectomy (TX) or sham operation was conducted by removal of the thyroid along with embedded parathyroids in control PT-*YFP;Dicer*$^{+/+}$ mice, or the thyroids with no intact parathyroid glands in PT-*YFP;Dicer*$^{-/-}$ mice, as illustrated by the dashed lines in representative fluorescent dissection microscope images. (**B**) Serum PTH levels 30

min post TX or sham operation. Results are presented as mean±SE. *, p<0.05. (**C**) Representative RNAscope analysis of 2-month-old control PT-*tdTomato;Dicer*$^{+/+}$ and PT-*tdTomato;Dicer*$^{-/-}$ mice depicting the expression of GCM2, Dicer, PTH and nuclear Dapi. n=2.

Figure 4. Identification of small parathyroid cell clusters in PT-*tdTomato;Dicer*$^{-/-}$ substituting intact glands early after birth. (**A**) Mice engineered to express both *YFP* and *tdTomato* exclusively in the parathyroids were examined by fluorescent guided microscopy of the exposed neck area at 3 months of age. Representative images from dissection microscopy for *YFP* or *tdTomato* display speckles of cell clusters by *tdTomato expression*, but not by *YFP* expression in the PT-*Dicer*$^{-/-}$ mouse. (**B**) Representative fluorescent dissection microscope images superimposed on bright field images of the exposed neck area in postpartum PT-*tdTomato;Dicer*$^{+/+}$ and PT-*tdTomato;Dicer*$^{-/-}$ mice at various ages. n=2-16. Magnification: P1 x2.5, P11-8 months x2. The right panels additionally exhibit a 5-fold magnification at 8 month. Arrows point to the location of parathyroid glands or cell clusters. T, thyroid; Tr, trachea. Fluorescence intensity exposure was set to 2 seconds for YFP and 0.25 seconds for tdTomato. (**C**) Intensity analysis of the tdTomato signal in parathyroid glands of PT-*tdTomato;Dicer*$^{+/+}$ control and PT-*tdTomato;Dicer*$^{-/-}$ *P1 mice* as shown in B, quantified using ImageJ software.

Figure 5. Parathyroid-specific PT-*Dicer* $^{-/-}$ mice have reduced phosphorylated pS6 levels in their parathyroids. (**A**) Representative Western blot showing phosphorylated pS6 (Ser235/236) (pS6) and α/β tubulin proteins from P1 PT-*YFP*;*Dicer* $^{+/+}$ and PT-*YFP*;*Dicer* $^{-/-}$ mice. Protein extracts from pooled microdissected parathyroid glands from 8-12 mice in each lane. (**B**) Quantitative assessment of pS6 normalized to α/β tubulin as shown in A. (**C**) Representative IF staining of paraffin sections from parathyroid glands of 3 month-old control PT-*Dicer* $^{+/+}$ and PT-*Dicer* $^{-/-}$ mice stained for nuclear sytox (green), PTH (blue) and pS6 (red). (**D**) Quantification of pS6 intensity, as shown in C, quantified using ImageJ software. *, p<0.05.

Figure 6. Parathyroid-specific *mTORC1*$^{-/-}$ mice exhibit disrupted parathyroid glands yet maintain normal serum PTH levels. (**A**) Representative fluorescent microscopy images of tdTomato fluorescence, superimposed on bright field images of the exposed parathyroids from control PT-*mTORC1*$^{+/+}$ and PT-*mTORC1*$^{-/-}$ mice at various postnatal stages. n=6-16. T, thyroid; Tr, trachea. Arrows point to the parathyroid glands or residual cell clusters. Fluorescence intensity exposure was set to

67 milliseconds and the magnification x2. (**B**) Histological sections stained with H&E from PT-*mTORC1*$^{+/+}$ and PT-*mTORC1*$^{-/-}$ mice. (**C**) Serum PTH levels in PT-*mTORC1*$^{+/+}$ and PT-*mTORC1*$^{-/-}$ mice at various ages.

Figure 7. PT-*TSC1*$^{-/-}$ mice have enlarged parathyroid glands from early after birth, decreased survival and increased serum PTH and calcium levels. (**A**) Survival probability curves based on Kaplan-Meier estimates of control PT-*TSC1*$^{+/+}$ ((blue) and PT-*TSC1*$^{-/-}$ (orange) mice at 1 month to 1 year. (**B**) Serum PTH at different ages. (**C**) Serum calcium measured using a Atellica™ CH Calcium assay. Only a single PT-*TSC1*$^{-/-}$ mouse that survived to 11 months is shown. (**D**) Representative fluorescence microscopy images for tdTomato, laid over bright field images of the exposed parathyroids from control PT-*TSC1*$^{+/+}$ and PT-*TSC1*$^{-/-}$ mice at different postnatal ages. n=3-14. T, thyroid; Tr, trachea. The fluorescence intensity exposure was 67 milliseconds and the magnification x1.9. The image of the PT-*TSC1*$^{-/-}$ mouse at 11 month shows only one of the 2 parathyroids at this magnification, due to their large size. (**E**) Parathyroid gland size as measured using ImageJ platform. *, $p<0.05$.

Figure 8. Parathyroid-specific *Dicer* and *TSC1* double knockout (PT-*Dicer*$^{-/-}$;*TSC1*$^{-/-}$) reverses the aparathyroidism of PT-*Dicer*$^{-/-}$ mice and restores their ability to increase PTH after CKD. (**A**) Representative fluorescent microscopy images of tdTomato fluorescence superimposed on bright field images of parathyroid glands in 2 month-old control (PT-*Dicer*$^{+/+}$;*TSC1*$^{+/+}$) mice and in mice with and parathyroid-specific *Dicer, mTORC1, TSC1, or TSC1* and *Dicer* double ablation. Exposure duration was 0.25 seconds. Arrows indicate parathyroid glands or cell clusters, T, thyroid, Tr, trachea. (**B**) Serum PTH levels in PT-*YFP*;*Dicer*$^{-/-}$ and PT-*Dicer*$^{-/-}$;*TSC1*$^{-/-}$ mice that were fed a control or an adenine-rich high phosphorus diet for 3 weeks to induce kidney failure and SHP. Results are presented as mean±SE. *, $p<0.05$ compared to PT-*YFP;Dicer*$^{+/+}$ control mice fed a control diet. #, $p<0.05$ compared to control mice with kidney failure. (**C**) Schematic representation illustrating the impact of *Dicer*, *mTORC1, TSC1* and combined *Dicer* and *TSC1* ablation on mTORC1 pathway activity and parathyroid gland structure. (**D**) Model outlining the relationship between Dicer, miRNA and the mTOR pathway. In normal basal conditions, Dicer facilitates miRNA maturation contributing to basal mTORC1 pathway activity, which is essential for maintaining intact parathyroid glands and the development of CKD induced SHP.

Supplemental Figure legends

Supplemental Figure 1. Parathyroid-specific deletion of *Dicer* and miRNA in the parathyroid does not affect the expression of PTH or cleaved caspase 3, nor the volume of the parathyroids at E19.5 and E21.5. (**A**) Representative IF staining for PTH and cleaved caspase 3 of parathyroids from control PT-*Dicer*$^{+/+}$ and PT-*Dicer*$^{-/-}$ embryos at both E19.5 (**B)** Similar IF staining images for parathyroids as in A at E21.5 (**C&D)** Quantitative volumetric assessment of parathyroids (PT-*Dicer*$^{+/+}$ n=4-7, PT-*Dicer*$^{-/-}$ n=5 parathyroids). The division into right and left glands is illustrated in panel D.

Supplementary Figure 2. PT-*YFP;Dicer*$^{-/-}$ mice have normal basal serum PTH, calcium and phosphate levels but a muted increase in serum PTH after adenine rich high-phosphorus diet-induced kidney failure. Control PT-*YFP;Dicer*$^{+/+}$ and PT-*YFP;Dicer*$^{-/-}$ mice were fed a control or an adenine-rich high phosphorus diet for 3 weeks to induce kidney failure and SHP. Serum levels of calcium (**A**), phosphate (**B**), urea nitrogen (BUN) (**C**) and PTH (**D**) were quantified. Data are presented as mean±SE. *, $p<0.05$ compared to PT-*YFP;Dicer*$^{+/+}$ control mice fed a control diet. #, $p<0.05$ compared to control mice with kidney failure.

Supplemental Figure 3. Analysis of control probes in parathyroid glands by RNAscope. Representative RNAscope analysis performed on parathyroid glands from 2 month-old control mice using positive and negative GCM2, Dicer and PTH probes and nuclear Dapi. n=2.

Supplemental Figure 4. N**o change in PTH content in parathyroids of PT-*mTORC1*$^{-/-}$ mice compared to control PT-*mTORC1*$^{-/-}$ mice**. (**A**) Representative IF PTH staining of paraffin sections from both control and PT-*mTORC1*$^{-/-}$ mice. (**B**) Quantification of the findings depicted in A and additional sections obtained from additional mice. *, $p<0.05$.

Supplemental Figure 5. Decreased PTH mRNA levels with unaltered CasR mRNA in PT-*mTORC1*$^{-/-}$ mice. RNA extracted from thyroparathyroid tissue of 3 month-old control PT-*mTORC1*$^{+/+}$ and PT-*mTORC1*$^{-/-}$ mice was analyzed for PTH and CasR mRNA levels by qRT-PCR, normalized against β-actin. *, $p<0.05$.

Supplemental Figure 6. Parathyroid-specific PT-*TSC1*$^{-/-}$ mice have increased p-S6 (Ser235/236) levels in their parathyroids. IF staining of parathyroid sections from control PT-*TSC1*$^{+/+}$ and PT-*TSC1*$^{-/-}$ mice highlighting pS6 (Ser235/236) (red)

and nuclear sytox (green). (**B**) Quantitative assessment of pS6 staining intensity, measured using ImageJ software. *, $p<0.05$.

Supplemental Figure 7. Visualization of parathyroid glands in a PT-*TSC1*$^{-/-}$ mouse under florescence microscopy for TdTomato displayed without magnification. The neck area of an 11 month PT-*TSC1*$^{-/-}$ mouse depicted in Figure 5A, and a control PT-*TSC1*$^{+/+}$ mouse at the same age, observed through fluorescence microscope for td-Tomato parathyroids at magnification x1.2 (left) and without magnification (right) demonstrating the size and intensity of the td-Tomato signal, which remains visible even without fluorescent light and no magnification.

Supplemental Figure 8. Representative fluorescence imaging for parathyroid gland size estimation in PT-*TSC1*$^{+/+}$ and PT-*TSC1*$^{-/-}$ mice, as shown in Figure 5B. Representative td-Tomato (left panels) and bright field images (right panels) used for estimating the size of parathyroid glands, outlined by broken lines and analyzed using ImageJ software. The left panels depict tdTomato florescence imaging at each age.

Figure 1

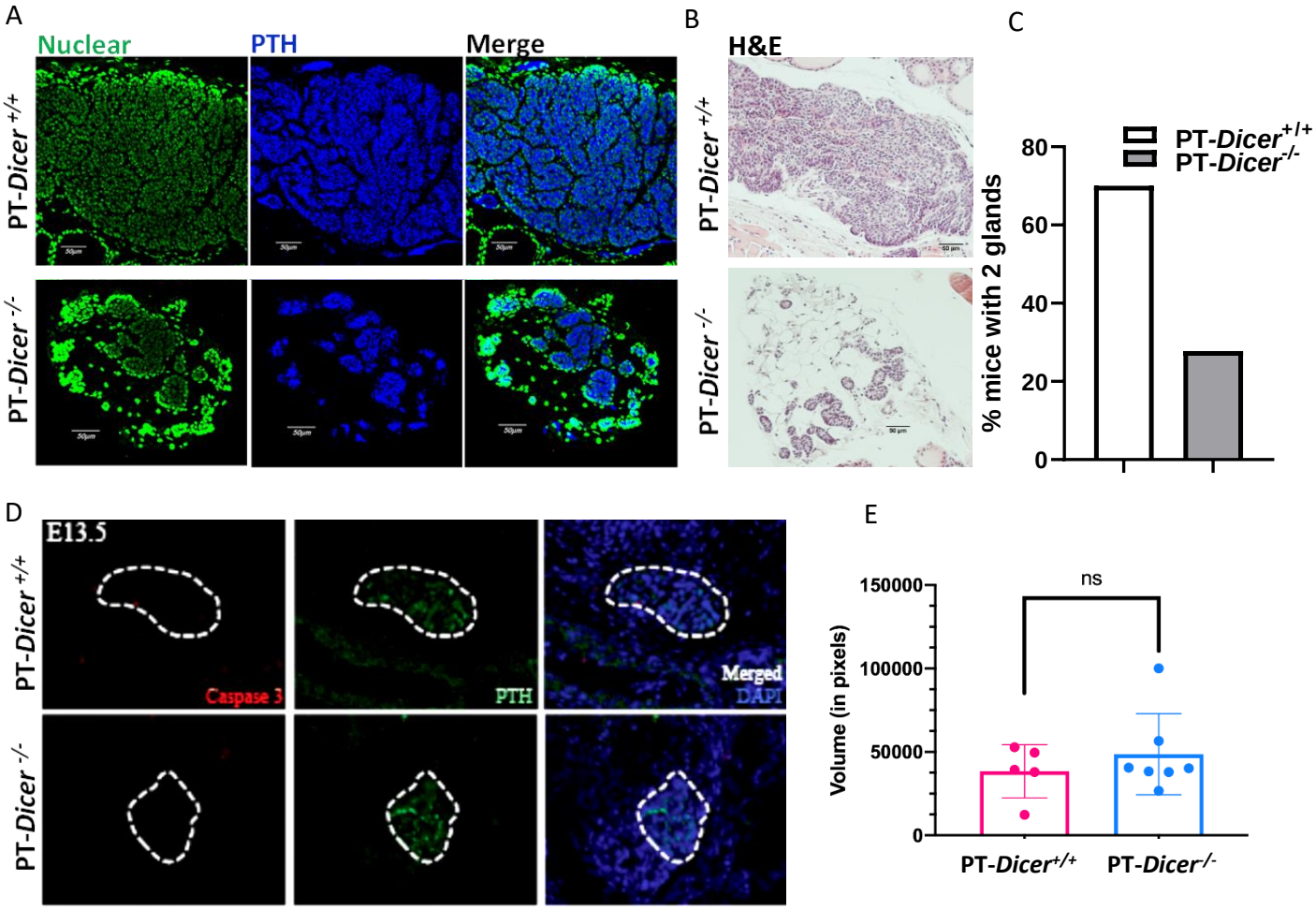
A
Nuclear
PTH
Merge
PT-Dicer +/+
PT-Dicer -/-
B
H&E
PT-Dicer +/+
PT-Dicer -/-
C
PT-Dicer+/+
PT-Dicer-/-
% mice with 2 glands
80
60
40
20
0
D
E13.5
Caspase 3
PTH
Merged
DAPI
PT-Dicer +/+
PT-Dicer -/-
E
ns
Volume (in pixels)
150000
100000
50000
0
PT-Dicer+/+
PT-Dicer-/-

Figure 2

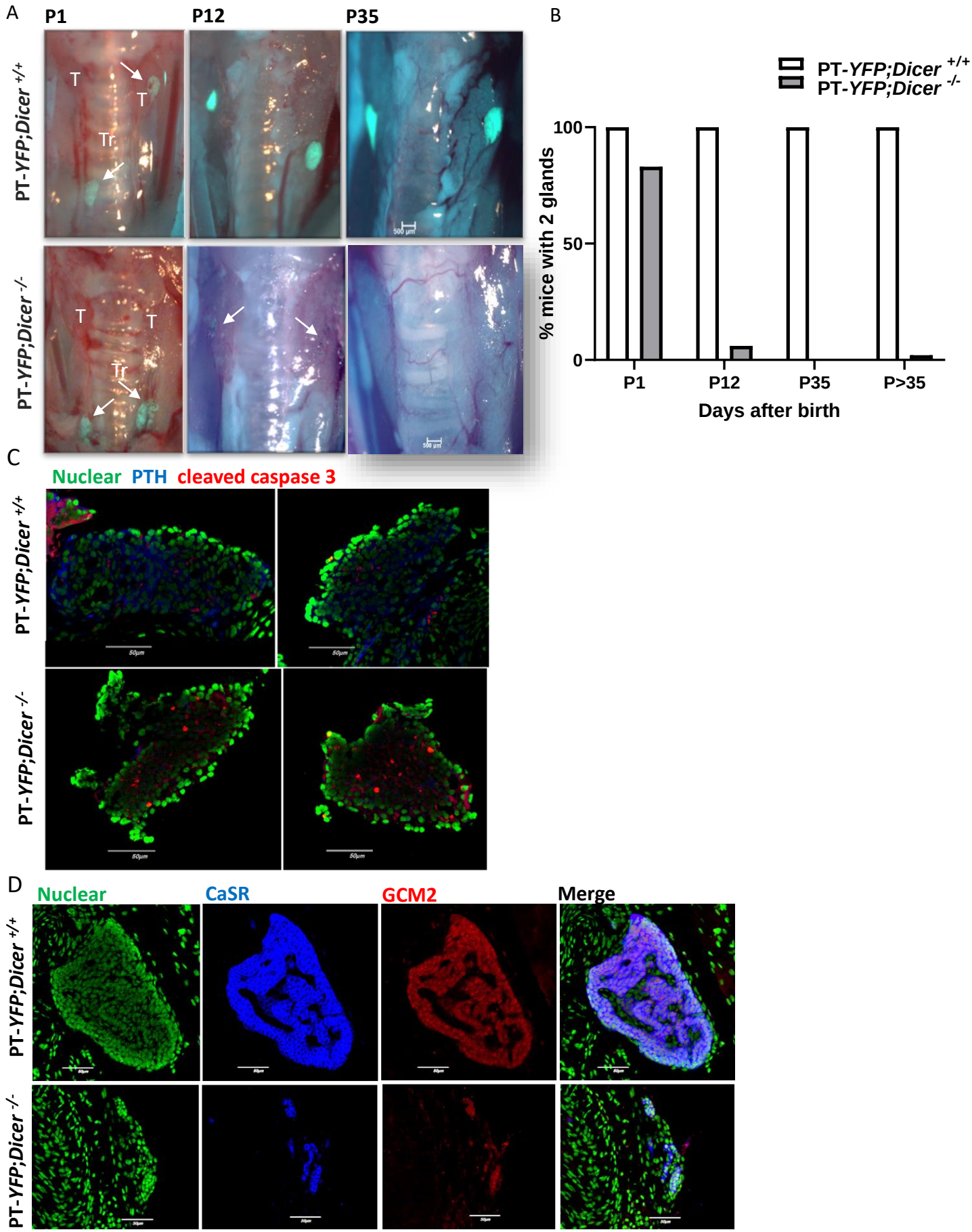
A
P1
P12
P35
PT-YFP;Dicer +/+
PT-YFP;Dicer -/-
T
Tr
500 µm
B
PT-YFP;Dicer +/+
PT-YFP;Dicer -/-
% mice with 2 glands
100
50
0
P1
P12
P35
P>35
Days after birth
C
Nuclear
PTH
cleaved caspase 3
50µm
D
Nuclear
CaSR
GCM2
Merge

Figure 3

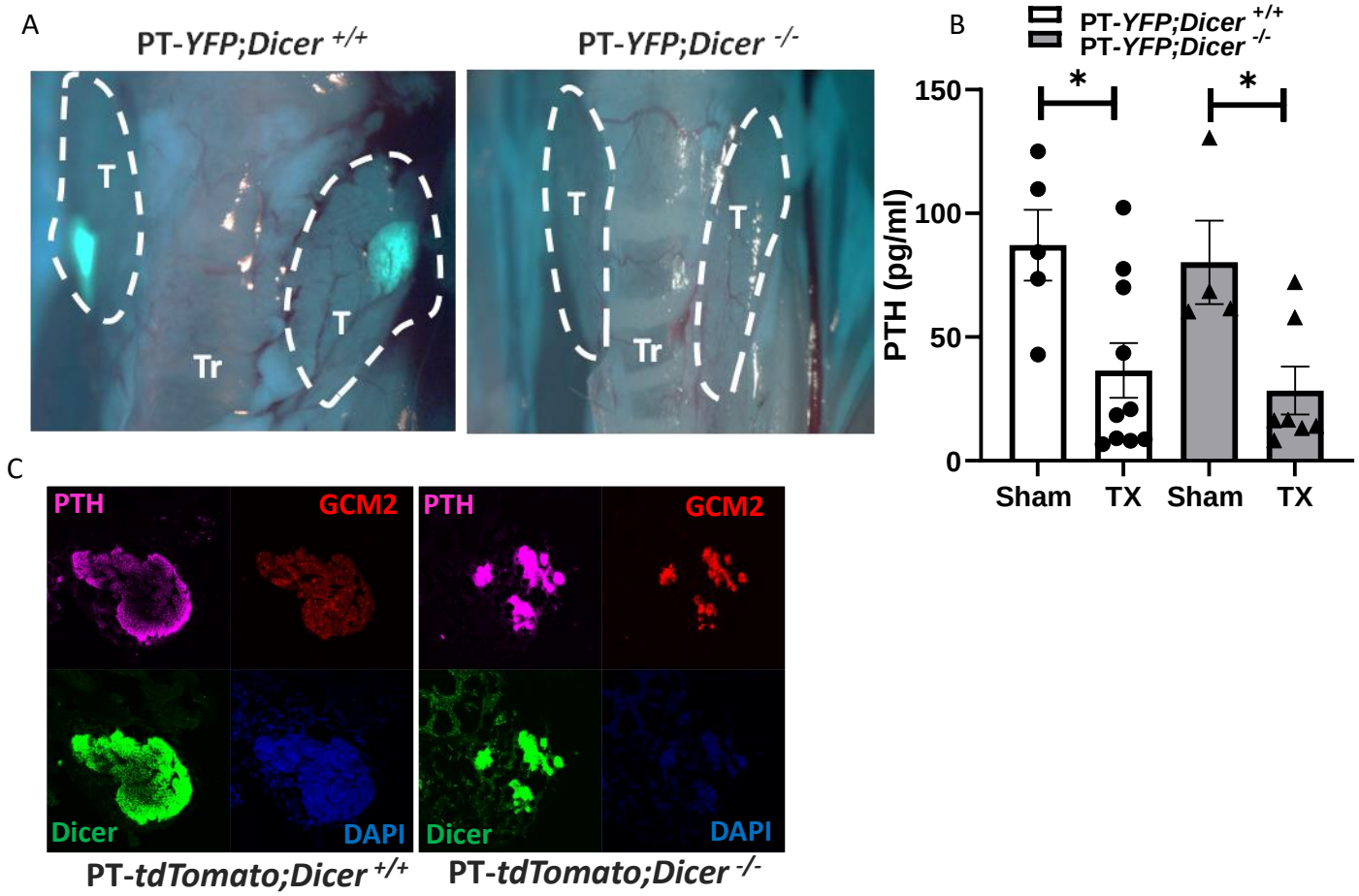
A
PT-YFP;Dicer +/+
PT-YFP;Dicer -/-
T
T
Tr
T
T
Tr
B
PT-YFP;Dicer +/+
PT-YFP;Dicer -/-
PTH (pg/ml)
150
100
50
0
*
*
Sham
TX
Sham
TX
C
PTH
GCM2
Dicer
DAPI
PTH
GCM2
Dicer
DAPI
PT-tdTomato;Dicer +/+
PT-tdTomato;Dicer -/-

Figure 4

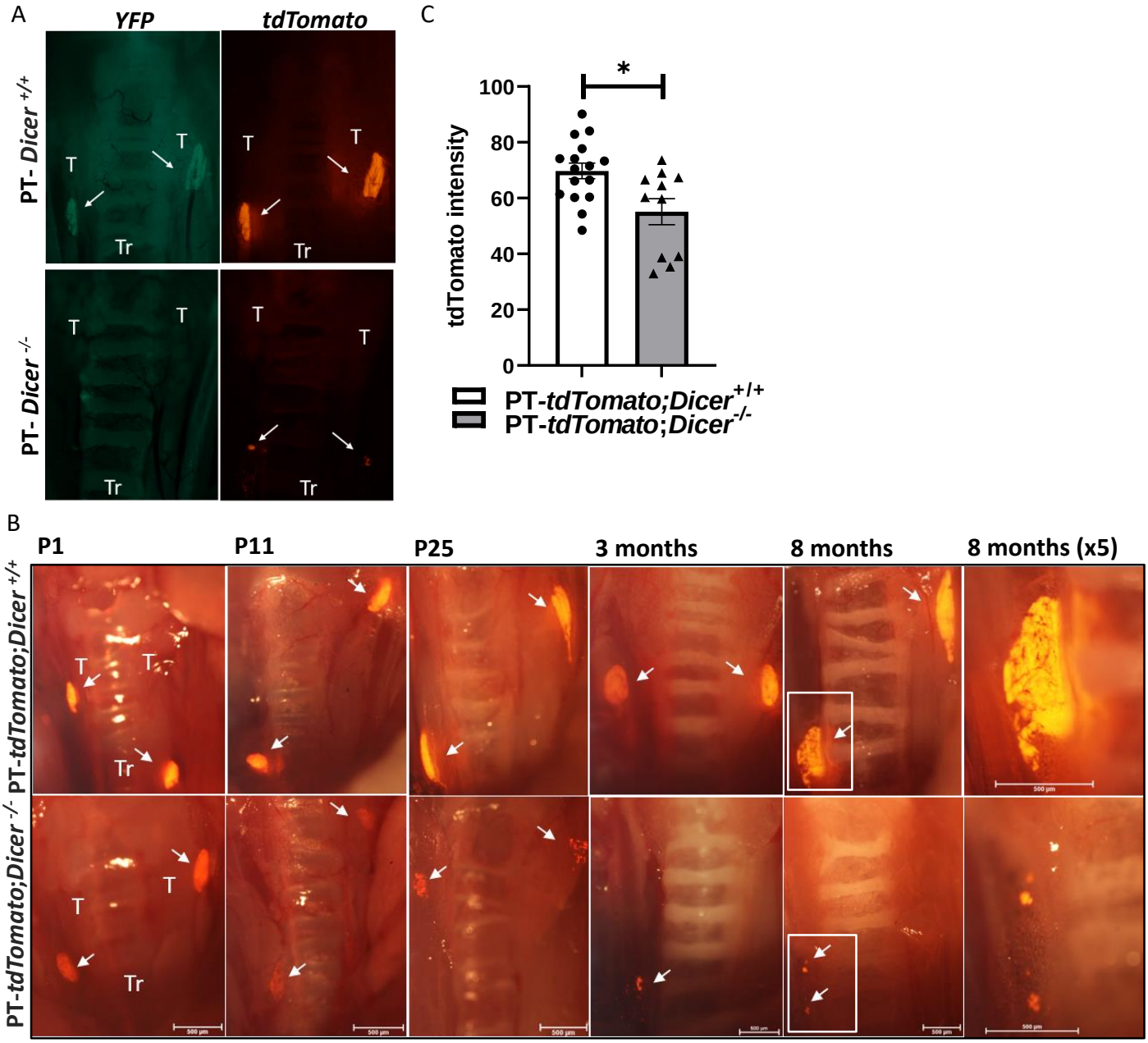
A
YFP
tdTomato
PT- Dicer +/+
PT- Dicer -/-
T
Tr
C
tdTomato intensity
100
80
60
40
20
0
*
PT-tdTomato;Dicer+/+
PT-tdTomato;Dicer-/-
B
P1
P11
P25
3 months
8 months
8 months (x5)
PT-tdTomato;Dicer +/+
PT-tdTomato;Dicer -/-
500 µm

Figure 5

A

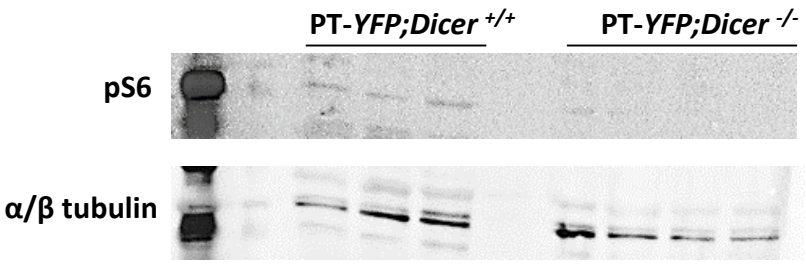

B

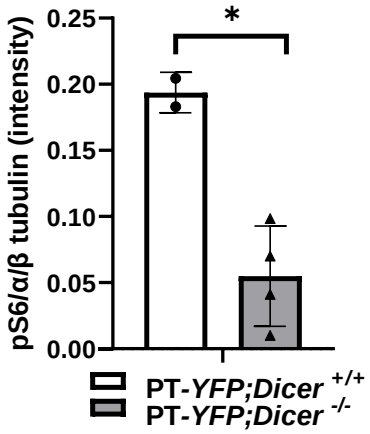

C

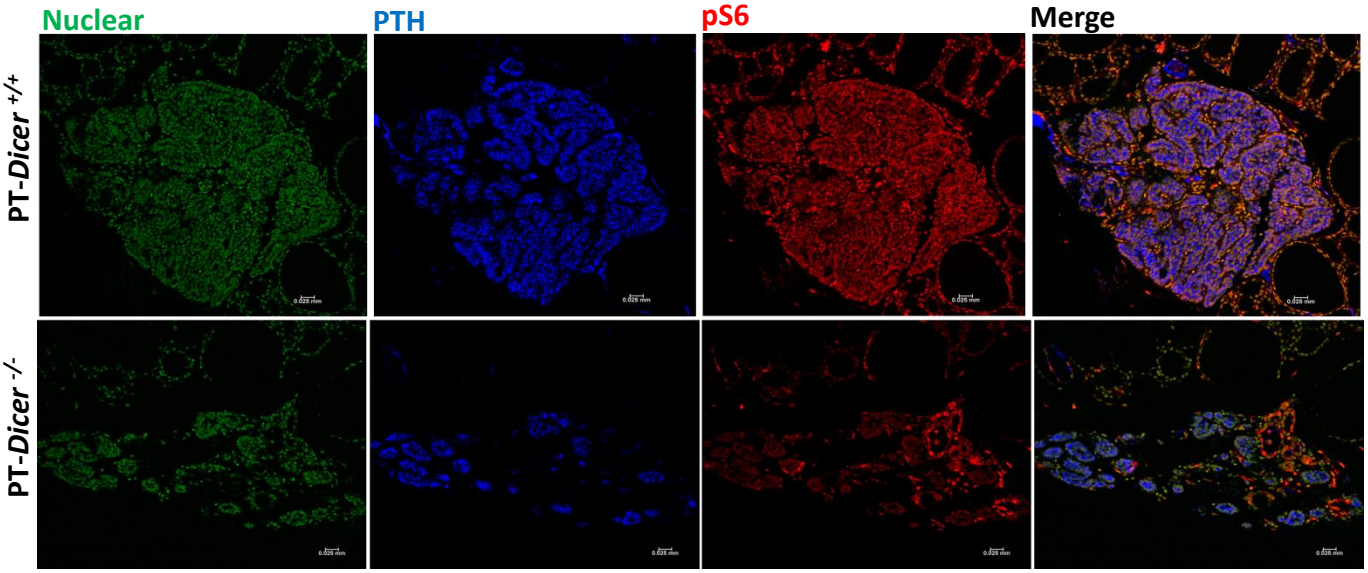

D

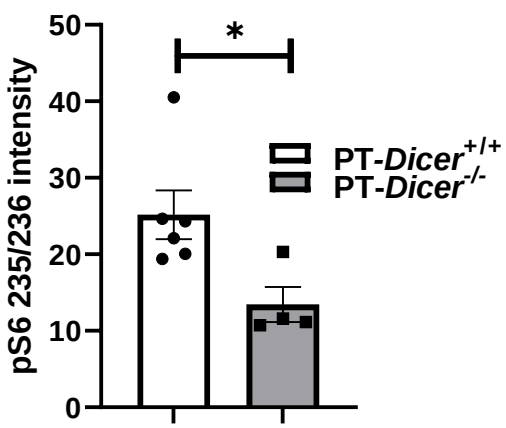

Figure 6

A

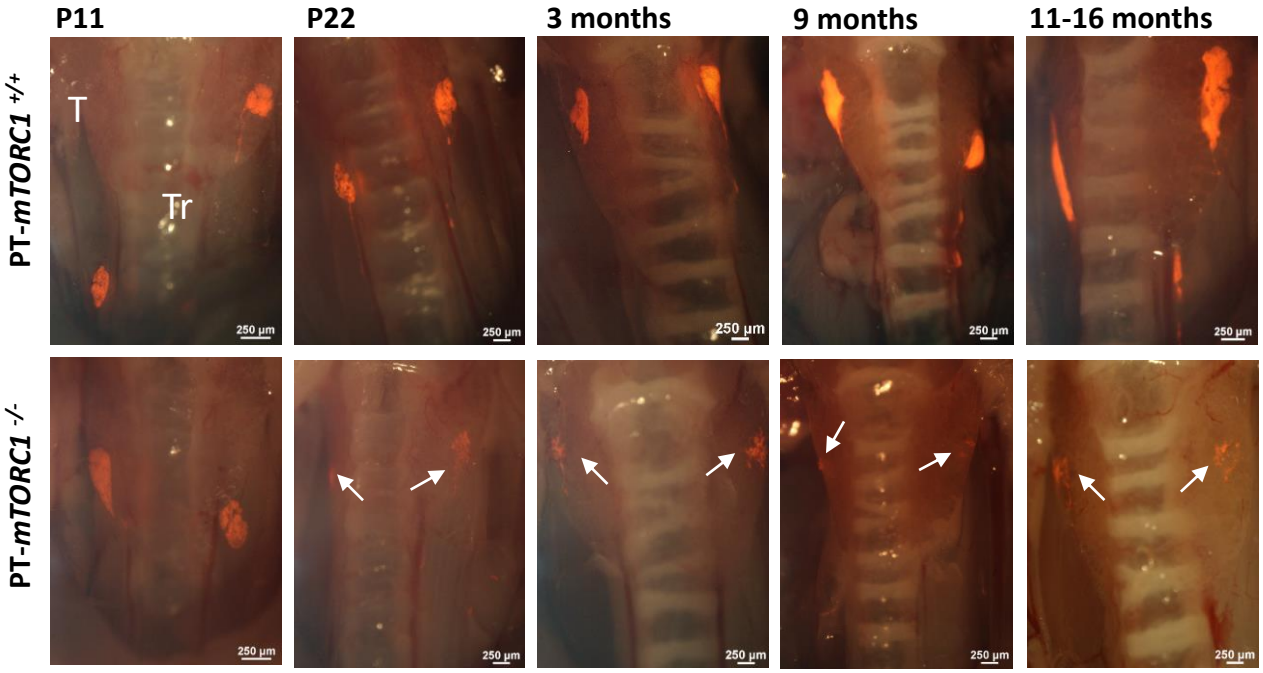
P11
P22
3 months
9 months
11-16 months
PT-mTORC1 +/+
PT-mTORC1 -/-
T
Tr
250 µm

B

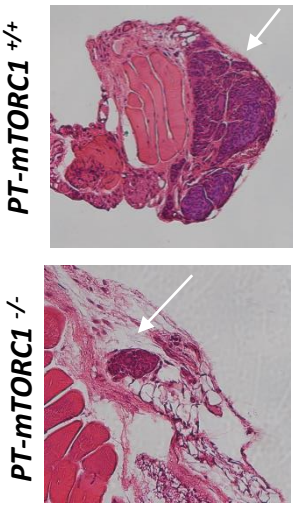
PT-mTORC1 +/+
PT-mTORC1 -/-

C

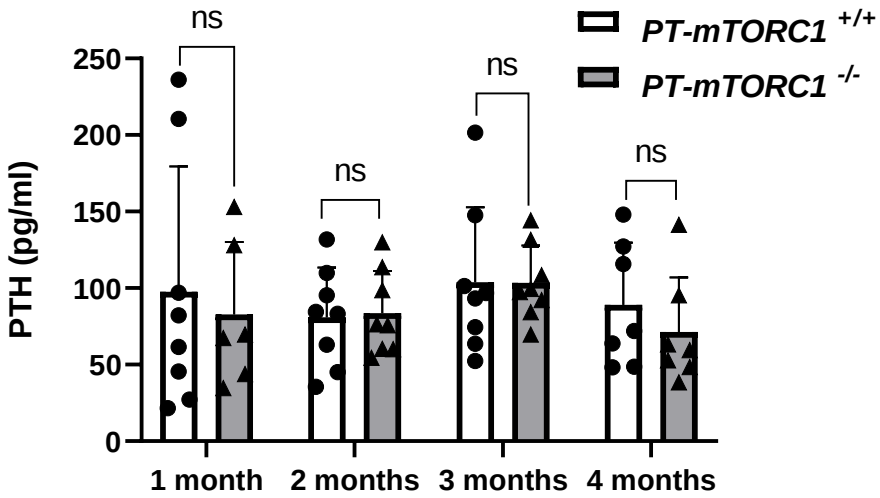
PT-mTORC1 +/+
PT-mTORC1 -/-
PTH (pg/ml)
250
200
150
100
50
0
ns
ns
ns
ns
1 month
2 months
3 months
4 months

Figure 7

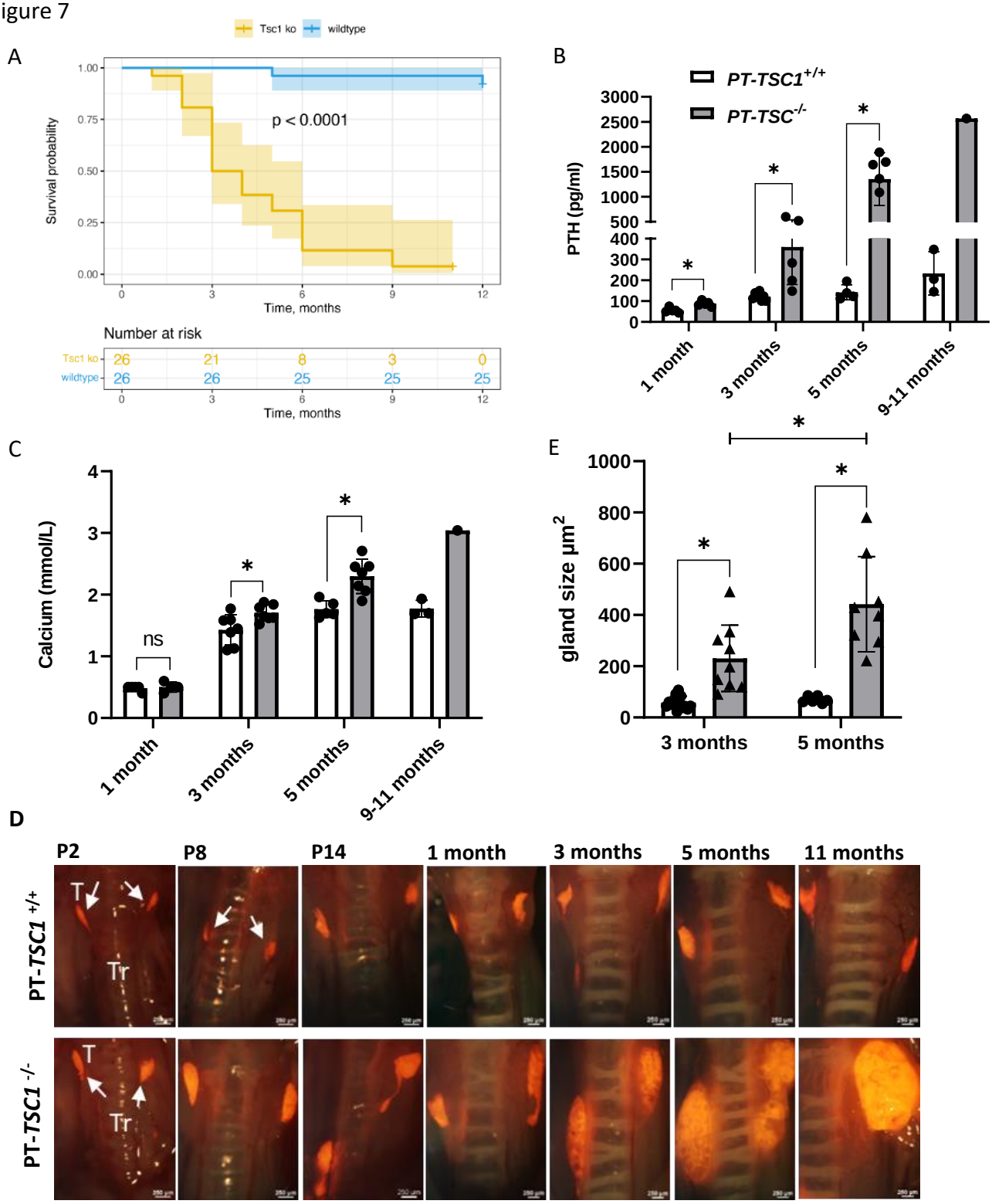
A
Tsc1 ko
wildtype
Survival probability
1.00
0.75
0.50
0.25
0.00
p < 0.0001
0
3
6
9
12
Time, months
Number at risk
Tsc1 ko 26 21 8 3 0
wildtype 26 26 25 25 25
Time, months
B
PT-TSC1+/+
PT-TSC-/-
PTH (pg/ml)
3000
2500
2000
1500
1000
500
400
300
200
100
0
*
1 month
3 months
5 months
9-11 months
C
Calcium (mmol/L)
4
3
2
1
0
ns
*
1 month
3 months
5 months
9-11 months
E
gland size µm2
1000
800
600
400
200
0
*
3 months
5 months
D
P2
P8
P14
1 month
3 months
5 months
11 months
PT-TSC1 +/+
PT-TSC1 -/-
T
Tr

Figure 8

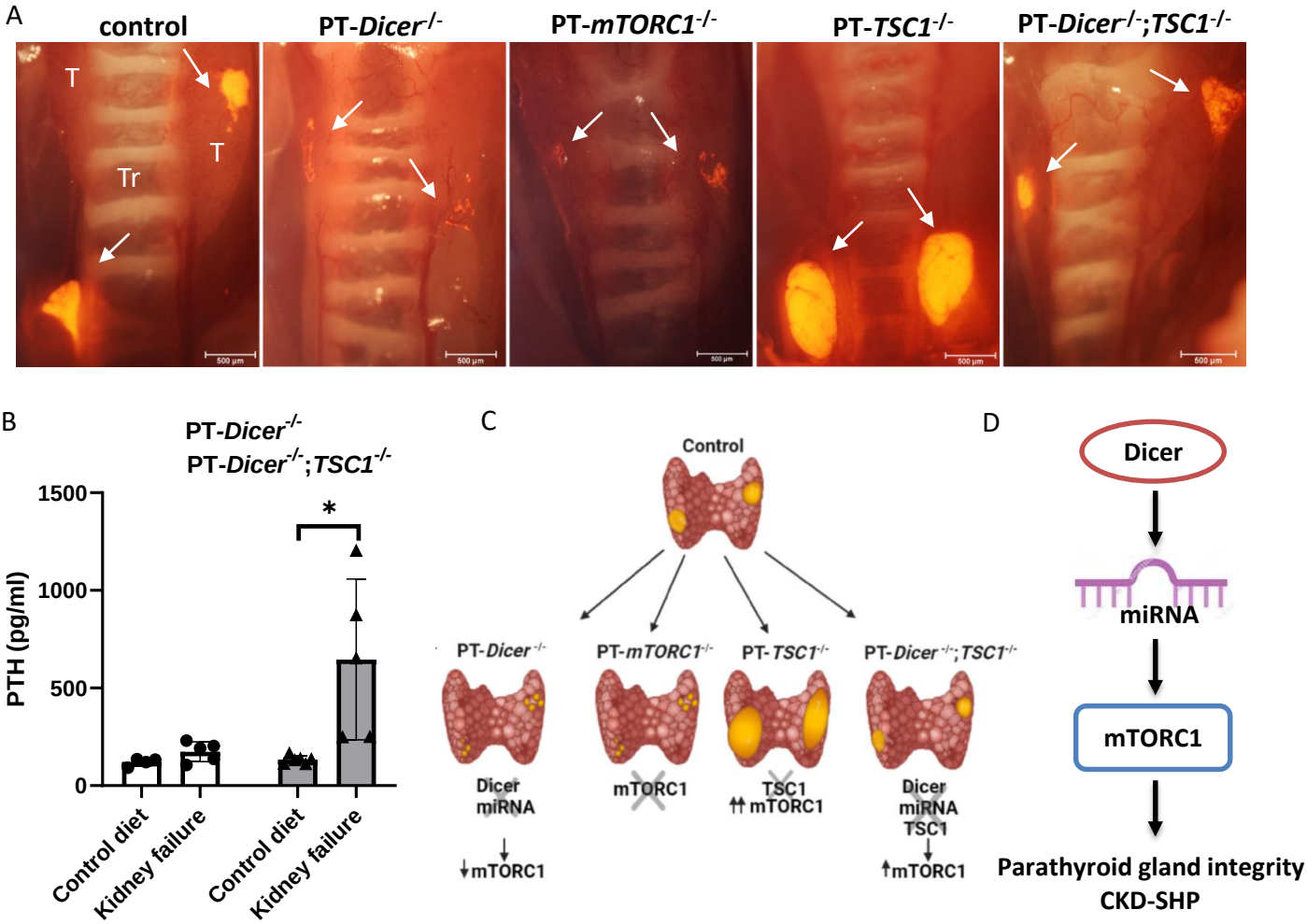
A
control
PT-Dicer-/-
PT-mTORC1-/-
PT-TSC1-/-
PT-Dicer-/-;TSC1-/-
T
T
Tr
B
PT-Dicer-/-
PT-Dicer-/-;TSC1-/-
PTH (pg/ml)
1500
1000
500
0
*
Control diet
Kidney failure
Control diet
Kidney failure
C
Control
PT-Dicer-/-
PT-mTORC1-/-
PT-TSC1-/-
PT-Dicer-/-;TSC1-/-
Dicer
miRNA
↓mTORC1
mTORC1
TSC1
↑↑ mTORC1
Dicer
miRNA
TSC1
↑mTORC1
D
Dicer
miRNA
mTORC1
Parathyroid gland integrity
CKD-SHP